

ENHANCEMENT OF THE PHOTOSTABILITY OF BLUE PHOSPHORESCENCE  
USING PLASMONIC SURFACES

By

KELSEY MORGAN GWYNNE

A thesis submitted to the

School of Graduate Studies

Rutgers, The State University of New Jersey

In partial fulfillment of the requirements

For the degree of

Master of Science

Graduate Program in Materials Science and Engineering

Written under the direction of

Deirdre M. O'Carroll

And approved by

---

---

---

---

New Brunswick, New Jersey

May, 2020

## **ABSTRACT OF THE THESIS**

Enhancement Of The Photostability Of Blue Phosphorescence Using Plasmonic Surfaces

by KELSEY MORGAN GWYNNE

Thesis Director:

Deirdre M. O'Carroll

Organic light-emitting devices (OLEDs) are used in flat panel displays such as televisions and cell phones. OLEDs have superior color purity, image quality, and flexibility, and less pixelation than traditional LCDs. OLEDs use fluorescent and/or phosphorescent materials in their emissive layer. Fluorescence emits from the singlet state, and can only emit up to 25% of the excitons. Phosphorescence can emit three times the amount of excitons as fluorescence due to its ability to emit from the singlet and triplet state, and therefore can emit 100% of the excitons, in theory. Although phosphorescence has greater efficiency than fluorescence, blue phosphorescent material is currently replaced in OLEDs with fluorescent material due to the instability of blue phosphorescent materials caused by triplet exciton quenching processes and chemicals. Various approaches have been developed to improve the stability of such phosphors including passivation, development of new organometallic molecules, and control of host-dopant composition in thin films. Here, we demonstrate an extrinsic approach to improving the photostability of blue organometallic phosphors that employs photoluminescence lifetime reductions caused by the local electric fields of plasmonic surfaces. We show that the decay rate of phosphorescence is increased on certain

plasmonic surfaces, which improves the stability of a common blue organometallic phosphor. This approach is distinctive because it involves modification to the local electromagnetic environment of the phosphor rather than modifications to the phosphor molecular structure or to the emitting material composition. Future studies will further examine the Purcell Effect's impact on blue phosphorescent materials using silver and gold discrete nanoparticles. More work should be done to confirm the mechanism increasing stability, and testing the blue organic phosphorescent material coated nanostructures in devices. For increased commercial and financial production feasibility, a large scale solution processing method should be created.

## **Acknowledgments**

This material is based upon work supported by the National Science Foundation (DMR-1554954). CDW and DMOC also acknowledge support from Science Foundation Ireland under Grant number 16/FRL/3870. The transient photoluminescence lifetime measurements were performed at the Center for Functional Nanomaterials, which is a U.S. DOE Office of Science Facility at Brookhaven National Laboratory under Contract No. DE-SC0012704. I would like to thank my collaborators Catrice M. Carter, Zeqing Shen, Zhongkai Cheng, and Rahma Leil for their contributions in sample fabrication, preparation, and sample testing (please refer to figure captions for individual contributions of collaborators). The individual contributions from each collaborator are acknowledged in the relevant figure caption in Chapter 2 and 3. I gratefully acknowledge the useful discussions and assistance from Kun Zhu and Prof. Jing Li. I would also like to thank my research group members Jill Tracey, Nasir Javed, Cindy Kumah, and Hemanth Maddali for their assistance and support throughout the study. I thank Dr. Evelyn Erenrich for her support and encouragement to pursue higher education, and for introducing me to Rutgers University. I also thank the School of Graduate Studies for honoring me with a SUPER Grad fellowship that supported my education and research. I would like to acknowledge and thank my committee members, Dr. Lisa Klein and Dr. Dunbar Birnie, for their time, commentary, and service on my committee. Lastly, I acknowledge and thank Dr. Deirdre M. O'Carroll for her constant support, insights, teachings, and feedback in addition to providing me the experience to work on this project and inspiration to attend graduate school. I am very grateful and appreciative to have Dr. O'Carroll as research director and mentor.

This thesis work is a continuation of work started by Dr. Catrice M. Carter and described in her PhD thesis [1]. Chapter 2 of this thesis, “PHOTOLUMINESCENCE STABILITY OF BLUE ORGANIC PHOSPHORESCENT MATERIALS ON SILVER NANOSTRUCTURED SURFACES” is a pending joint publication with Kelsey Gwynne and Catrice Carter as joint first authors. Both first authors equally contributed to the manuscript that is included in the second chapter. The authors are anticipating that sections of the future work may be published in the future as well after more future work is completed. All contributions from collaborators were specified at the relevant points in the thesis captions below.

My specific contributions include: designing and developing thin film preparation methods (PVK:FIrpic host/dopant selection, PVK:FIrpic solution concentration and preparation method, optimization of PVK:FIrpic film thickness, preliminary measurements for NPT size dependence, and preliminary PL data for Ag/Au discrete NPT study), developing microscopy methods for stability measurements (PL set-up using an epifluorescence microscope, PL stability data collection [low and high power], power dependence analysis, transmittance factor, PL stability data analysis and fitting, PL stability, and transmittance adjusted stability), characterization of thin film properties (UV-Vis absorbance and transmittance), and manuscript preparation (creating graphics for the paper, revising the paper, and conducting a literature review).

## Table of Contents

<b>ABSTRACT OF THE THESIS</b>	<b>ii</b>
<b>Acknowledgments</b>	<b>iv</b>
<b>List of Tables</b>	<b>vii</b>
<b>List of Figure Captions</b>	<b>viii</b>
<b>List of Acronyms</b>	<b>xiv</b>
<b>Chapter 1: INTRODUCTION</b>	<b>1</b>
1.1. Excitons in OLEDs	2
1.2. Unstable Blue Phosphorescence	3
1.4. Motivation for This Work	4
1.5. Interactions between Emitters and Metals	5
1.6. Selection of Materials	6
1.7. References	8
<b>Chapter 2: PHOTOLUMINESCENCE STABILITY OF BLUE ORGANIC PHOSPHORESCENT MATERIALS ON SILVER NANOSTRUCTURED SURFACES</b>	<b>10</b>
2.1. Abstract	10
2.2. Introduction	11
2.3. Results	13
2.3.1. Extrapolation to an OLED Device:	31
<b>2.4. Conclusions</b>	<b>33</b>
<b>2.5. Methods</b>	<b>33</b>
2.5.1. Preparation Organic Thin Films and Surfaces	33
2.5.2. Characterization of Organic Thin Films:	37
2.5.3. Photoluminescence Characterization Methods	39
2.6. References	45
<b>Chapter 3: FUTURE WORK</b>	<b>48</b>
3.1. Preliminary Data	48
3.2. Methods	49
3.2.1. Sample Preparation	49
3.2.2. Optical Characterization and Spectroscopy	51
3.3 References	53
<b>Chapter 4: OUTLOOK</b>	<b>54</b>

## List of Tables

**Table 2.1. (page 25)** - The average PL lifetime ( $\tau_{PL}$ ), intensity at time,  $t, = 0$  s, shortest PL lifetime decay component ( $\tau_1$ ), longer PL lifetime decay component ( $\tau_2$ ), and the longest PL lifetime decay component ( $\tau_3$ ) for PVK:FIrpic thin films on glass, planar Ag, 1.6  $\mu\text{m}$  1-D Ag grating, 0.7  $\mu\text{m}$  1-D Ag grating, NPT Ag metasurfaces and NPO Ag metasurfaces. The PL lifetime components were extracted from fits to the data using a second or third order exponential decay functions. The percentage contributions of each lifetime component to the average PL lifetime are shown in parentheses.

**Table 2.2. (page 27)** - The excitation power corrected  $L_{90}$  stability enhancements (i.e.,  $E_{90}^T$ ), average PL lifetime ( $\tau_{PL}$ ), PL intensity enhancement ( $E_{PL}$ ) of PVK:FIrpic thin films on various Ag surfaces, and radiative decay rate enhancement ( $E_r$ ). Two different excitation power densities were employed for the stability measurements: 13.6  $\text{mW}/\text{cm}^2$  and 136  $\text{mW}/\text{cm}^2$ . Some  $E_{90}^T$  data was collected by Catrice Carter.

## List of Figure Captions

**Figure 1.1. (pg 1)** - An example of phosphorescence is glow in the dark stars (a), reproduced from Ref. [6]. When excitation light is turned off, the stars emit light until they run out of stored energy. These inorganic phosphors, such as the commonly-used Zinc Sulfide, demonstrate phosphorescence [7,8]. Fluorescence emits light quickly. An example of fluorescence can be seen in some light bulbs (b), reproduced from Ref. [9]. In an OLED device structure (c), organic fluorescent and/or phosphorescent material are used to create its emissive layer [10].

**Figure 1.2. (pg 3)** - The greater energy needed to emit from the singlet state compared to the triplet state can be visualized in this Jablonski diagram [13]. Through intersystem crossing, phosphorescence is able to emit excitons (excited electron-hole pairs) that were in the singlet and triplet states. Light is emitted when excitons relax, or move down to the ground state ( $S_0$ ) from the excited state ( $S_{1+x}$  and  $T_{1+x}$  where  $x \geq 0$ ) [15].

**Figure 1.3. (pg 6)** - (a) Exciton dissociation is depicted with a positive charged metal attracting electrons from the exciton to dissociate. (b) Dipole-dipole coupling in which dipoles and their reflections in the metal (image dipoles) line up and cause quenching. (c) LSPRs occur at further distances from the surface, and cause enhancement of emission or absorption.

**Figure 2.1. (pg 14)** - (a-c) Schematics of Ag surfaces: (a) NPT Ag; (b) NPO Ag; (c) 1-D Ag grating (nominal period of 0.7  $\mu\text{m}$ ). (d-f) SEM images of fabricated NPT Ag, NPO



Ag and 1-D Ag grating surfaces, respectively. The insets in (d-f) are dark-field back-scattered light images of the corresponding surfaces. The scale bar in the insets is 10  $\mu\text{m}$ . Nanoparticles were created by Zeqing Shen. Other surfaces and all other sample preparation shown above are by Catrice Carter. SEM and Dark Field imaging performed by Catrice Carter.

**Figure 2.2. (pg 16)** - (a) Molecular structures of PVK and FIrpic. (b) Energy level diagram showing  $S_1$ ,  $T_{1,S}$ ,  $T_{1,E}$ , and  $S_0$  energy levels of PVK and FIrpic derived from Ref. [29, 30]. (c) Absorbance spectra (dashed curves) and intensity-normalized photoluminescence spectra (solid curves) of the host PVK, the dopant FIrpic, and the 9:1 blend PVK:FIrpic. A drop cast film of FIrpic was used to obtain the absorption spectrum of FIrpic (see Methods). All other spectra were obtained from spin coated thin films. Data obtained by Catrice Carter and Rahma Leil. (d) Transmission spectra of PVK:FIrpic-coated Ag surfaces and of PVK:FIrpic-coated planar Ag. The yellow bar indicates the excitation wavelength range used for PL stability measurements. The average of two measurements was used for each transmission spectrum. All spectra were baselined at 900 nm except the NPT sample which is baselined at  $\sim 420$  nm. A small irregularity at 400 nm (the lamp crossover wavelength) occurred in all the spectra, due to a difference in the relative lamp intensities during the measurements.

**Figure 2.3. (pg 18)** - PL intensity versus UV exposure time for PVK:FIrpic thin films on glass substrates with and without passivation by epoxy and glass. Data acquired by Rahma Leil.

**Figure 2.4. (pg 19)** - (a) Representative accelerated PL stability test of PVK:FIrpic thin films on various Ag surfaces. For the PL stability measurements, all samples were continuously exposed to focused UV light (wavelength  $365 \text{ nm} \pm 12 \text{ nm}$ ), with a power density of  $136 \text{ mW/cm}^2$  for 1 hour. The measured data is represented by symbols and exponential fits to the data are represented by the solid lines. No correction was carried out for differences in excitation power caused by variations in sample transmittance at the excitation wavelength. (b) PL images of PVK:FIrpic coated Ag surfaces, at 20x magnification, acquired before (top row) and after (bottom row) stability measurements using the same conditions as (a). All images have the same image acquisition time and settings, and all images are on the same scale; the scale bar is  $200 \text{ }\mu\text{m}$ . (c) Average stability enhancements ( $E_{90}^T$ ) averages (points) and standard deviations (error bars) for PVK:FIrpic coated Ag surfaces at two excitation powers  $13.6 \text{ mW/cm}^2$  and  $136 \text{ mW/cm}^2$ . For a particular excitation power the stability enhancement was normalized to the transmittance of the sample at the excitation wavelength (to correct for slight variations in excitation power due to differences in the transmittance of the samples); see Equation 1. The average  $E_{90}^T$  values were obtained from numerous stability measurements of each sample type as follows: four measurements of the  $1.6 \text{ }\mu\text{m}$  1-D Ag grating, five measurement of the  $0.7 \text{ }\mu\text{m}$  1-D Ag grating, five measurements of the NPO Ag, and three measurements of the NPT Ag at  $13.6 \text{ mW/cm}^2$ . Two stability measurements of each Ag surface type were used at  $136 \text{ mW/cm}^2$ . (d) Transient PL lifetime decay curves of PVK:FIrpic thin films on various surfaces. A  $372 \text{ nm}$  picosecond pulsed laser was

employed for excitation and the measurements were carried out in reflection mode (Fig. 5). PL lifetime measurements were performed by Zeqing Shen.

**Figure 2.5. (pg 20)** - Schematic of experimental configuration used for transient PL lifetime measurements.

**Figure 2.6. (pg 21)** - Transmittance spectra for different Ag (meta)surfaces with/without a PVK:FIrpic coating. All samples except the uncoated 1.6  $\mu\text{m}$  1-D Ag grating were baselined at 900 nm. The uncoated 1.6  $\mu\text{m}$  1-D Ag grating was baselined at  $\sim 425$  nm.

**Figure 2.7. (pg 22)** – Transmittance for PVK:FIrpic coated Ag (meta)surfaces at a wavelength of 365 nm.

**Figure 2.8. (pg 23)** - Transmittance for uncoated Ag (meta)surfaces at a wavelength of 365 nm.

**Figure 2.9. (pg 28)** - (a) Excitation-power-corrected accelerated PL stability curves of PVK:FIrpic thin films on various NPT Ag surfaces with different nominal NPT sizes and on planar Ag (50 nm). For the PL stability measurements, all samples were continuously exposed to focused UV light (wavelength  $365\text{ nm} \pm 12\text{ nm}$ ), with a power density of  $136\text{ mW/cm}^2$  for 1 hour. The PL stability curves were raised to the power of  $T$  (the transmission correction factor), to correct for small differences in excitation power due to variations in sample transmittance at the excitation wavelength; see Methods. Data is

represented by symbols and exponential fits to the data are represented by the solid lines. Nanoparticle fabrication performed by Zhongkai Cheng. (b) Scattered light spectra of PVK:FIrpic coated NPT Ag surfaces and planar Ag (solid curves). Also shown is the photoluminescence spectrum of a PVK:FIrpic film for comparison (dashed curve). The scattering spectrum of the 20 nm NPT surface was multiplied by a factor of 10 to show the shape of the spectrum. Dark field spectra conducted by Rahma Leil.

**Figure 2.10. (pg 30)** - Transmittance spectra for (a) PVK:FIrpic coated NPT metasurfaces of varying NPT diameter (nominally, 20 nm, 80 nm and 150 nm), and (b) uncoated NPT metasurfaces of varying NPT diameter. Also shown is the transmittance of corresponding planar Ag samples. All spectra are baselined at 900 nm except the 150 nm sample, which is baselined at ~475 nm. The total thickness of Ag deposited on all surfaces was 50 nm.

**Figure 2.11. (pg 40)** - Schematic of the sample configurations used for the PL stability measurements. Two stability configurations were used. One was in epifluorescence mode, where 365 nm Hg arc lamp excitation was incident on the glass/epoxy/emitter side of the sample and the emission was collected from the same side of the sample (as shown above). The other configuration was in transmission mode, where 355 nm laser excitation was employed on the glass/epoxy/emitter side of the sample (as before), and the emission was collected from the opposite side of the sample (i.e., the metal/glass side). The epoxy was a UV-curable optical adhesive (NOA 63, Norland Products Inc.).

**Figure 3.1. (pg 49)** - Photoluminescence stability measurements at 100,000 cd/m<sup>2</sup>.

**Figure 3.2. (pg 50)** - Discrete Ag NPT sample schematic.

## List of Acronyms

OLEDs - Organic Light Emitting Devices

LCDs - Liquid Crystal Displays

QLEDs - Quantum dot Light Emitting Devices

Ph-OLEDs - Phosphorescent Organic Light Emitting Devices

LSPR - Localized Surface Plasmon Resonance

FIrpic - bis[2-(4,6-difluorophenyl)pyridinato- $C^2,N$ ](picolinato)iridium(III)

PVK - poly(N-vinylcarbazole)

IQE - Internal Quantum Efficiency

TTA - Triplet-Triplet Annihilation

TPA - Triplet-Polaron Annihilation

UV-Vis - Ultraviolet-Visible

NPT - Nanoparticle

NPO - Nanopore

PL - Photoluminescence

AFM - Atomic Force Microscopy

QY - Quantum Yield

PAA - Poly(Acrylic) Acid

## Chapter 1: INTRODUCTION

Organic light-emitting devices (OLEDs) are used in next-generation flat panel displays such as televisions, cell phones, and tablets. They are classified as organic due to their use of organic semiconducting materials as the emissive layer. While OLEDs can be expensive to manufacture due to a lack of large scale solution processing methods, OLEDs have many advantages. OLEDs are more flexible, thinner, less pixelated on large screens, and have better color purity than inorganic light-emitting devices and liquid crystal displays (LCDs) [2,3]. OLEDs also use less energy for black/dark pixels (a pure black due to an absence of light) compared to LCDs and Quantum dot light emitting devices (QLEDs) as they do not require a black light. There are two types of photoluminescence (light emission) used for OLEDs, fluorescence and phosphorescence. Unlike its green and red counterparts, blue phosphorescent materials are unstable and are consequently replaced by less efficient, but stable blue fluorescent material [4,5].



**Figure 1.1.** An example of phosphorescence is glow in the dark stars (a), reproduced from Ref. [6]. When excitation light is turned off, the stars emit light until they run out of stored energy. These inorganic phosphors, such as the commonly-used Zinc Sulfide, demonstrate phosphorescence [7,8]. Fluorescence emits light quickly. An example of fluorescence can be seen

in some light bulbs (b), reproduced from Ref. [9]. In an OLED device structure (c), organic fluorescent and/or phosphorescent material are used to create its emissive layer [10].

### 1.1. Excitons in OLEDs

Excitons are Coulombically-bound electron-hole pairs that are excited optically or electrically in semiconductor materials with low dielectric constants, such as organics. Singlet excitons are the primary type of exciton excited under optical excitation (i.e., by absorption of high energy photons). In contrast, the excitons that form in the OLED's emissive layer are electrically excited and have spins that are associated with either singlet excitons (total spin,  $S=0$ ) or triplet excitons (total spin,  $S=1$ ), leading to fluorescence or phosphorescence emission, respectively. Exciton spin is important because it affects how well photons are emitted from excited states of the material [11]. Fluorescence is emitted from radiative recombination of singlet excitons, and can emit up to 25% of electrically excited excitons. The rest of its excitons are trapped in non-radiative triplet states, and as a result, electrically excited fluorescent OLEDs can achieve one-third of the efficiency of phosphorescent OLEDs, in theory (Fig. 1.2) [4]. Phosphorescence is emitted from triplet excitons. However, through intersystem crossing, triplet excitons can be excited indirectly from the excited singlet exciton state (Fig. 1.2). Under optical excitation only singlet excitons are directly excited. However, under electrical excitation both singlet and triplet states are excited. Furthermore, since there are three triplet states for every singlet state, electrically-driven phosphorescent OLEDs (Ph-OLEDs) can emit three times more light than fluorescent OLEDs, in theory, and have the ability to emit with 100% internal quantum efficiency (Fig. 1.2) [4,5,12,13]. Triplet state emission is typically non-radiative for organic materials; however, the addition of small



fractions of a heavy metal, such as iridium to the organic molecular structure, creates spin-orbit coupling. This causes mixing of singlet and triplet states and enables direct (radiative) emission from the triplet state and, therefore, effective phosphorescent emission [10]. For over a decade, scientists have been making progress in improving phosphorescent light emitting materials' emission to be closer to the theoretical internal quantum efficiency value.

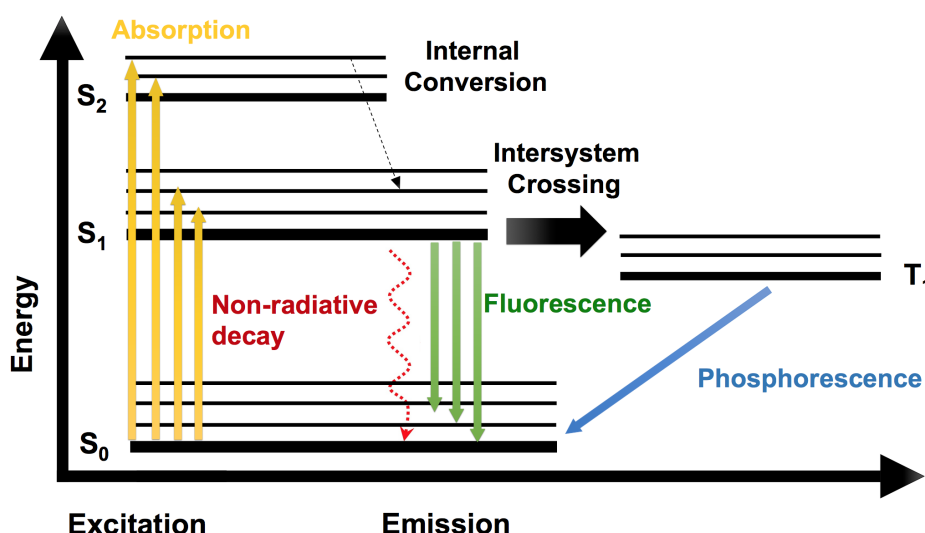


**Figure 1.2.** The greater energy needed to emit from the singlet state compared to the triplet state can be visualized in this Jablonski diagram [13]. Through intersystem crossing, phosphorescence is able to emit excitons (excited electron-hole pairs) that were in the singlet and triplet states. Light is emitted when excitons relax, or move down to the ground state ( $S_0$ ) from the excited state ( $S_{1+x}$  and  $T_{1+x}$  where  $x \geq 0$ ) [15].

## 1.2. Unstable Blue Phosphorescence

Blue phosphorescent OLED materials are unstable due to triplet-triplet annihilation and triplet polaron quenching processes that occur in the emissive layer

[3,4,12]. Since triplet excitons remain in the excited state for a long time ( $\sim 1 \mu\text{s}$  for FIrpic) before recombining radiatively (emitting light), occasional exciton-exciton collisions occur that cause triplet exciton quenching. As a result, this causes a decrease in the material's light-emission efficiency over time [15]. This effect becomes particularly pronounced at high excitation powers. To reduce such losses, many researchers manipulate host and dopant materials and alter or add device layers [2,16]. Our focus, however, is on using silver nanostructures embedded in the organic phosphorescent emissive layer to reduce and/or prevent the triplet-triplet annihilation and triplet quenching.

### **1.3. The Purcell Effect using Plasmonic Nanostructures**

Noble metals, like silver, gold, and copper, have unique properties that increase light outcoupling efficiency and the quantum yield of light-emitting devices. The single electron in silver's s-orbital will not interact with its full d-orbital, and therefore electron mobility is increased [17]. The free-electron also allows for high electrical and thermal conductivity [17]. Strong localized electromagnetic fields are created when noble metals are nanostructured, and are typically referred to as plasmonic modes [17]. These localized electromagnetic fields can increase the probability of spontaneous emission and decrease recombination time from nearby molecules [18,19,20]. This phenomenon is called the Purcell effect.

### **1.4. Motivation for This Work**

In this work, we hypothesize that due to the Purcell effect, phosphorescent OLED

material will interact with a silver nanostructure's strong localized electric field and will cause the OLED material to emit light more quickly. We anticipate that this will increase the photostability of the OLED material because, if the material is in the excited state for less time, then triplet quenching opportunities are reduced. In our case, we embed nanostructured silver into the phosphorescent light-emitting material to reduce and/or prevent triplet quenching. Therefore, we anticipate that the shortened emission lifetime caused by the Purcell Effect will increase stability.

### **1.5. Interactions between Emitters and Metals**

Shortened emission lifetime can be attributed to the enhancement of either radiative or non-radiative decay. If radiative decay is enhanced more than non-radiative decay, emission intensity will increase, and if non-radiative decay is enhanced more than radiative decay, it causes more quenching of emission (intensity to decrease). Additionally, there is a distance dependence. It is well known that quenching of emission occurs within 5 nm of metal (charge transfer or dipole-dipole interaction in which the dipoles are mirror images), but it cannot explain lifetime shortening at long distances (enhancement due to plasmonic electric field interactions). Charge transfer occurs in the short-range ( $\sim 1-2$  nm) and causes excitons to dissociate and electrons and/or holes (depending on the metal surface's charge) transfer to the metal surface (Figure 1.3). This results in exciton quenching. Another quenching mechanism is energy transfer in the longer range ( $\sim 1-10$  nm), in which excitons interact with the metal surface by dipole-dipole coupling (Figure 1.3). Localized surface plasmon resonances (LSPRs) which occur in low loss metals such as noble metals, however, cause enhanced emission or absorption,

depending on wavelength, at large distances from the metal surface (5-100 nm) (Figure 1.3).

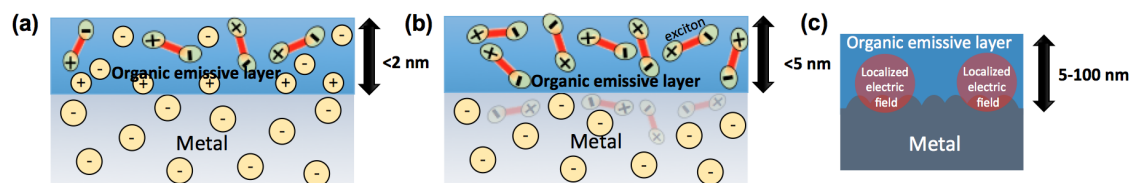


**Figure 1.3.** (a) Exciton dissociation is depicted with a positive charged metal attracting electrons from the exciton to dissociate. (b) Dipole-dipole coupling in which dipoles and their reflections in the metal (image dipoles) line up and cause quenching. (c) LSPRs occur at further distances from the surface, and cause enhancement of emission or absorption.

## 1.6. Selection of Materials

The emissive films used for this study are 60 nm thick, so we expect both radiative and non-radiative changes due to the interactions with the metals (i.e, non-radiative transfer to the metal is only a small contributor to the lifetime); see prior section. While we argue that both radiative and non-radiative decay rate enhancement occur due to the metal metasurfaces, our focus is on shortening the total phosphorescence lifetime and an overall stability increase. Therefore, either type of decay rate enhancement is expected to contribute to stability enhancement. Creating stable blue phosphorescent light will reduce an OLEDs' operation energy, which will lower the cost to operate the device. Stable blue phosphorescent light emission is also essential to create a better quality white light (red, green, and blue light together), and replace the blue fluorescent material that is currently being used in its place [2,3]. In this study, the emissive layer we employ contains the commonly-used blue phosphorescent dopant

bis[2-(4,6-difluorophenyl)pyridinato- $C^2,N$ ](picolinato)iridium(III) (FIrpic) and a host, poly(N-vinylcarbazole) (PVK), which have been used together in various studies [4,15,20]. The host, PVK, was chosen because it is commonly used in the optoelectronic field with the blue phosphorescent dopant, FIrpic [5,16,21]. The host improves light emission and assists in energy transfer through Dexter and Förster transfer processes while the dopant provides color and increases intersystem crossing [22,23]. Dexter energy transfer is short-range, transfers energy from the host to the dopant through intermolecular electron exchanges [11]. Förster energy transfer is long-range, non-radiative, couples host and dopant molecules (dipole-dipole) [11]. The dopant, an organometallic complex, provides spin-orbit coupling, and its localized magnetic field causes interactions with its electrons' spin, causing energy level shifts which enables phosphorescence (emission from the triplet state) [22,23].

Since energy is transferred from the host to the dopant, the  $T_1$  of PVK (host) should be greater than or equal to the  $T_1$  of FIrpic (dopant). PVK is an unusual host because it has two triplet states. Its higher energy triplet state,  $T_{1,S}$ , the triplet single-molecule state, is -2.8 eV. This is higher energy than FIrpic's  $T_1$  state of -3.1 eV [24,25]. PVK's second triplet state,  $T_{1,E}$ , the triplet excimer state, has less energy due to intermolecular interactions. The triplet excimer state is -3.3 eV [24,25]. Although it has two triplet states, since PVK's  $T_{1,S}$  has more energy than FIrpic's  $T_1$ , and because PVK is a commonly used host, its use with FIrpic in this work is supported.

## 1.7. References

- 1) Carter, C. Device and Metasurface Designs For Next-generation Blue-emitting Organic LEDs: Cost, Sustainability, Efficiency, and Stability. PhD Thesis, *Rutgers University*. (2018).
- 2) Gather, M. C., Koehnen, A., Meerholz, K. White organic light-emitting diodes. *Advanced Materials* **23**, 233-248 (2011).
- 3) Jiang, W., Duan, L., Qiao, J., Dong, G., Zhang, D., Wang, L., Qiu, Y. High-triplet-energy tri-carbazole derivatives as host materials for efficient solution-processed blue phosphorescent devices. *Journal of Materials Chemistry*. **21**, 4918-4926 (2011).
- 4) Liu, H., Bai, Q., Yao, L., Hu, D., Tang, X., Shen, F., et al. Solution-processable hosts constructed by Carbazole/PO substituted tetraphenylsilanes for efficient blue electrophosphorescent devices. *Advanced Functional Materials*. **24**, 5881-5888 (2014).
- 5) Tao, Y., Yang, C., Qin, J. Organic host materials for phosphorescent organic light-emitting diodes. *Chemical Society Reviews*. **40**, 2943-2970 (2011).
- 6) Glow stickers. *Zeppy.io*, Web.
- 7) Helmenstine, A. How Glow in The Dark Stars Work. *Science Notes*. Web. (2015).
- 8) Glow in the dark - how does it work? *The Glow Company*, Web.
- 9) Speer-Williams, J. Stock Up on Incandescent Light Bulbs: In Fact, Buy a Lifetime Supply of Them. Web. (2016).
- 10) Chan, J., Rakic, A., Kwong, C., Djurisic, A.B., Majewski, M.L., Chan, Wai; Chui, P. Optimization of Organic Light Emitting Diode Structures. *Proceedings of SPIE - The International Society for Optical Engineering*. **5277**, 311-319 (2004).
- 11) Tanaka, I., Tokito, S. Energy-Transfer Processes between Phosphorescent Guest and Fluorescent Host Molecules in Phosphorescent OLEDs. *Highly Efficient OLEDs with Phosphorescent Materials*, 283-309 (2007).
- 12) Qian, Y., Cao, F., Guo, W. High thermal stability 3, 6-fluorene-carbazole-dendrimers as host materials for efficient solution-processed blue phosphorescent devices. *Tetrahedron*. **69**, 4169-4175 (2013).
- 13) Zhang, Y., Ding, L., Liu, X., Jiang, Z., Chen, H., Ji, S., et al. Spiro-fused N-phenylcarbazole-based host materials for blue phosphorescent organic light-emitting diodes. *Organic Electronics*. **20**, 112-118 (2015).
- 14) Photophysics of fluorescent proteins. *Institut de Biologie Structurale*, 1. Web. (2017).
- 15) Wang, J.; Zhang, H., Ji, W., Zhang, H., Zhu, F. Origin of efficiency roll-off for FIrpic based blue organic light-emitting diodes and implications on phosphorescent molecule design. *Jpn. J. Appl. Phys. Japanese Journal of Applied Physics*. **54**, 101601 (2015).
- 16) Su, S., Takahashi, Y., Chiba, T., Takeda, T., Kido, J. Structure-property relationship of pyridine-containing triphenyl benzene electron-transport materials

- for highly efficient blue phosphorescent OLEDs. *Advanced Functional Materials*. **19**, 1260-1267 (2009).
- 17) Russell, A. M., Lee, K. L. Structure-property relations in nonferrous metals. *Hoboken: Wiley-Interscience*. 302 (2005).
  - 18) Romeira, Bruno, Fiore, A. Purcell Effect in the Stimulated and Spontaneous Emission Rates of Nanoscale Semiconductor Lasers. *IEEE Journal of Quantum Electronics*. **54**, 1-12 (2018)
  - 19) Purcell, E. M. Spontaneous emission probabilities at radio frequencies, *Phys. Rev. Lett.* **69**, 681 (1946).
  - 20) Morozov, K. M., Ivanov, K. A., de Sa Pereira, D. et al. Revising of the Purcell effect in periodic metal-dielectric structures: the role of absorption. *Sci Rep.* **9**, 9604 (2019).
  - 21) Ma, D., Duan, L., Qiu, Y. Toward highly efficient blue organic light-emitting diodes: Fabricating a good-quality emissive layer cast from suitable solvents. *Dalton Transactions*. **45**, 6118-6123 (2016).
  - 22) O'Brien, D. F., Baldo, M. A., Thompson, M. E., Forrest, S. R. Improved energy transfer in electrophosphorescent devices. *Applied Physics Letters*. **74**, 442-444 (1999).
  - 23) Baldo, M. A., Lamansky, S., Burrows, P. E., Thompson, M. E., Forrest, S. R. Very high-efficiency green organic light-emitting devices based on electrophosphorescence. *Applied Physics Letters*. **75**, 4-6 (1999).
  - 24) Chaudhuri, D., Li, D., Sigmund, E., Wettach, H., Höger, S., Lupton, J. M. Plasmonic surface enhancement of dual fluorescence and phosphorescence emission from organic semiconductors: effect of exchange gap and spin-orbit coupling. *Chem. Commun.* **48**, 6675-6677 (2012).
  - 25) Ji, W., Zhang, L., Xie, W. Improving efficiency roll-off in phosphorescent OLEDs by modifying the exciton lifetime. *Opt. Lett.* **37**, 2019-2021 (2012).

## **Chapter 2: PHOTOLUMINESCENCE STABILITY OF BLUE ORGANIC PHOSPHORESCENT MATERIALS ON SILVER NANOSTRUCTURED SURFACES**

### **2.1. Abstract**

Organometallic phosphors are vital materials for high-efficiency organic light-emitting diodes used in display and lighting applications. However, problems of low photostability arise for blue-emitting phosphors due to chemical and environmental degradation, and to triplet quenching processes. Various approaches have been developed to improve the stability of such phosphors including passivation, development of new organometallic molecules, and control of host-dopant composition in thin films. Here, we demonstrate an extrinsic approach to improving the photostability of blue organometallic phosphors that employs photoluminescence lifetime reductions caused by the local electric fields of plasmonic surfaces. We show that the decay rate of phosphorescence is increased on certain plasmonic surfaces, which improves the stability of a common blue organometallic phosphor. This approach is distinctive because it involves modification to the local electromagnetic environment of the phosphor rather than modifications to the phosphor molecular structure or to the emitting material composition.



## 2.2. Introduction

Phosphorescent organic light-emitting diodes (Ph-OLEDs) can emit with up to 100% internal electroluminescence quantum efficiency (IQE) due to the use of organometallic phosphors as light-emitting dopants [1-7]. However, when operating blue emitting Ph-OLEDs at high luminances, a significant decrease in device efficiency occurs during operation over time [8,9]. Extensive work has been carried out to understand the causes of efficiency degradation with the main causes attributed to: (1) photooxidation; (2) an imbalanced hole-electron current; (3) triplet-triplet exciton annihilation (TTA); and (4) triplet-polaron annihilation (TPA) [8-13]. Development of effective processing and passivation strategies have mitigated the presence of oxygen in such devices to the point where photooxidation is no longer the main loss mechanism. The non-radiative quenching processes TTA and TPA have been ascribed to be the primary loss mechanisms in efficiency at high luminance [8-13]. TTA occurs when there is an accumulation of triplet excitons in a high-energy excited state due to the long lifetime of the emitting triplet state, while TPA occurs when an excited polaron state pairs with a triplet exciton and in both instances the excess energy is lost by thermalization [8-14].

Scientists and engineers have developed various methods to address the instability of blue PhOLEDs including: use of double emission layers [15,16]; alternative high mobility electron transport layers [15,17]; mixed host structures [13,18]; and development of organometallic phosphorescent molecules with short triplet lifetimes [9]. However, additional strategies are needed because stabilities of blue organometallic phosphors (~5000 h) still significantly lag those of red and green phosphors and of high-efficiency inorganic blue emitting materials. TTA is proportional to the square of triplet

exciton density, and the TPA scales with the triplet exciton density [17,18]. During operation, the exciton density is proportional to the exciton lifetime [17,19]. Hence, one way to address the efficiency roll-off issue is to accelerate the radiative decay rate (i.e., to decrease the radiative lifetime) of the triplet excitons in phosphorescent OLED materials.

This study aims to experimentally investigate the use of silver plasmonic surface films to increase the radiative decay rate of triplet exciton emission from blue phosphorescent films. Using this extrinsic approach, we hypothesize that the stability of blue phosphors can be improved. The reasoning behind our hypothesis is as follows: strong localized electromagnetic fields are created when noble metals, such as silver, are nanostructured which increases the local density of optical states in the near-field (i.e., within 100 nm) of the metal (plasmonic behavior). By increasing the available local density of optical states that the excitons in the triplet state of the phosphorescent emitter can couple to, the radiative decay rate will increase (the Purcell Effect) [20-25], thus, reducing the probability of triplet exciton quenching and increasing the phosphorescence stability [26]. This approach is different from the other approaches that have been developed to improve the stability of blue phosphorescent materials because it is an extrinsic approach that involves modification of the local electromagnetic environment of the phosphorescent thin films rather than modifications to the molecular structure or composition of the thin film. It is important to note that while both radiative and non-radiative decay are likely present, we are interested in the overall increase in stability, so either decay type should improve stability.

### 2.3. Results

The purpose of this study is to investigate if Ag plasmonic surfaces can modify the stability of blue phosphorescent OLED (Ph-OLED) materials. For this study, we used the host poly(N-vinylcarbazole) (PVK) with the blue phosphorescent dopant bis[2-(4,6-difluorophenyl)pyridinato- $C^2,N$ ](picolinate)iridium(III) (FIrpic), which are commonly-used in Ph-OLEDs [14,27,28]. This host-dopant matrix has been shown to improve light out coupling and enhance triplet excitation because the host assists in charge transport and excitation energy transfer, while the dopant provides color and increases intersystem crossing, which improves the internal quantum efficiency [14,27,28]. A blend solution containing the host and dopant was spin coated onto different Ag surfaces: nanoimprinted periodic 1-D Ag gratings (one with a nominal period of 1.6  $\mu\text{m}$ , and another with a nominal period of 0.7  $\mu\text{m}$ ), aperiodic nanoporous (NPO) Ag, and aperiodic nanoparticle (NPT) Ag (Fig. 2.1a-f); see Methods. For comparison, the blend solution was also spin coated onto planar silver.

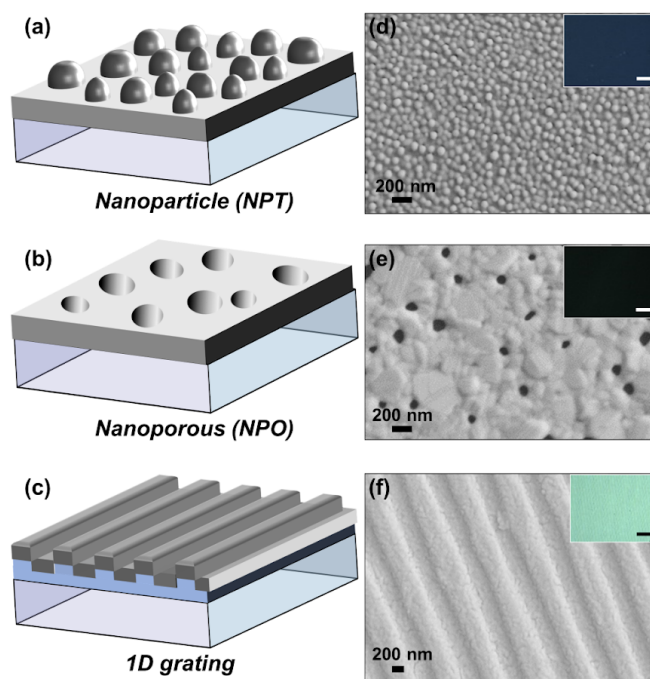


**Figure 2.1.** (a-c) Schematics of Ag surfaces: (a) NPT Ag; (b) NPO Ag; (c) 1-D Ag grating (nominal period of  $0.7\ \mu\text{m}$ ). (d-f) SEM images of fabricated NPT Ag, NPO Ag and 1-D Ag grating surfaces, respectively. The insets in (d-f) are dark-field back-scattered light images of the corresponding surfaces. The scale bar in the insets is  $10\ \mu\text{m}$ . Nanoparticles were created by Zeqing Shen. Other surfaces and all other sample preparation shown above are by Catrice Carter. SEM and Dark Field imaging performed by Catrice Carter.

The scanning electron microscope (SEM) images of the NPT surfaces show dense ( $\sim 140\ \text{particles}/\mu\text{m}^2$ ), quasi-hemispherical-shaped nanoparticles on their surface with an average diameter of  $62\ \text{nm} \pm 11\ \text{nm}$ . The NPO Ag surfaces had sparse ( $\sim 1\ \text{pore}/\mu\text{m}^2$ ), irregularly-shaped pores, approximately  $50\ \text{nm}$  to  $200\ \text{nm}$  in size, and the Ag regions between the pores had a polycrystalline appearance with Ag grains  $\sim 200\ \text{nm}$  in size. The 1-D Ag gratings showed regular ridges with periods like that of the expected nominal periods of  $1.6\ \mu\text{m}$  and  $0.7\ \mu\text{m}$  (Fig. 2.1f). Both 1-D Ag gratings exhibited small fissures in the Ag (less than  $200\ \text{nm}$  in size) superimposed on the grating pattern.

The characteristic absorption and normalized PL spectra for thin films of neat PVK, neat FIrpic and the PVK:FIrpic blend on glass are shown in Figure 2.2a; see Methods. The chemical structures of PVK and FIrpic are shown in Figure 2.2a, inset. The photoluminescence spectrum of PVK:FIrpic follows the characteristic FIrpic spectrum exhibiting two peaks at 472 nm and 500 nm, thus signifying proper energy transfer from the host, PVK, to the dopant, FIrpic. The peak absorption intensity of PVK is at approximately 350 nm, which is slightly red shifted from the expected PVK peak at a wavelength of 342 nm [5]. However, there is spectral overlap of the absorption spectrum of the dopant, FIrpic, and the photoluminescence spectrum of the host, PVK, in the wavelength range between 400 nm to 470 nm, which accounts for the efficient energy transfer. Energy is transferred from the host to the dopant, so the  $T_1$  of the host should be greater or equal to the  $T_1$  of the dopant. PVK is an abnormal host because its triplet state is separated into two. The  $T_{1,S}$  triplet single molecule state is 2.8 eV, which is higher than our dopant's  $T_1$  state of 3.1 eV [29,30]. When intermolecular interactions occur, the  $T_{1,S}$  energy is reduced to  $T_{1,E}$ . The  $T_{1,E}$  triplet excimer state is 3.3 eV [29,30]. PVK is a commonly used host, and its higher  $T_{1,S}$  state supports its use with FIrpic.

The 1-D Ag gratings, NPT Ag, and NPO Ag surfaces were all chosen due to their potential to increase light emission of PVK:FIrpic through resonant light scattering or through local electric-field enhancement at the emission wavelength. The transmittance spectra of the Ag surfaces show peaks from 300 nm to 350 nm due to the bulk plasma frequency of Ag (Fig. 2.2c). The coated NPT and NPO Ag surfaces exhibited reduced transmission compared to the coated planar Ag, whereas the coated 1-D Ag gratings exhibited increased transmission across the entire

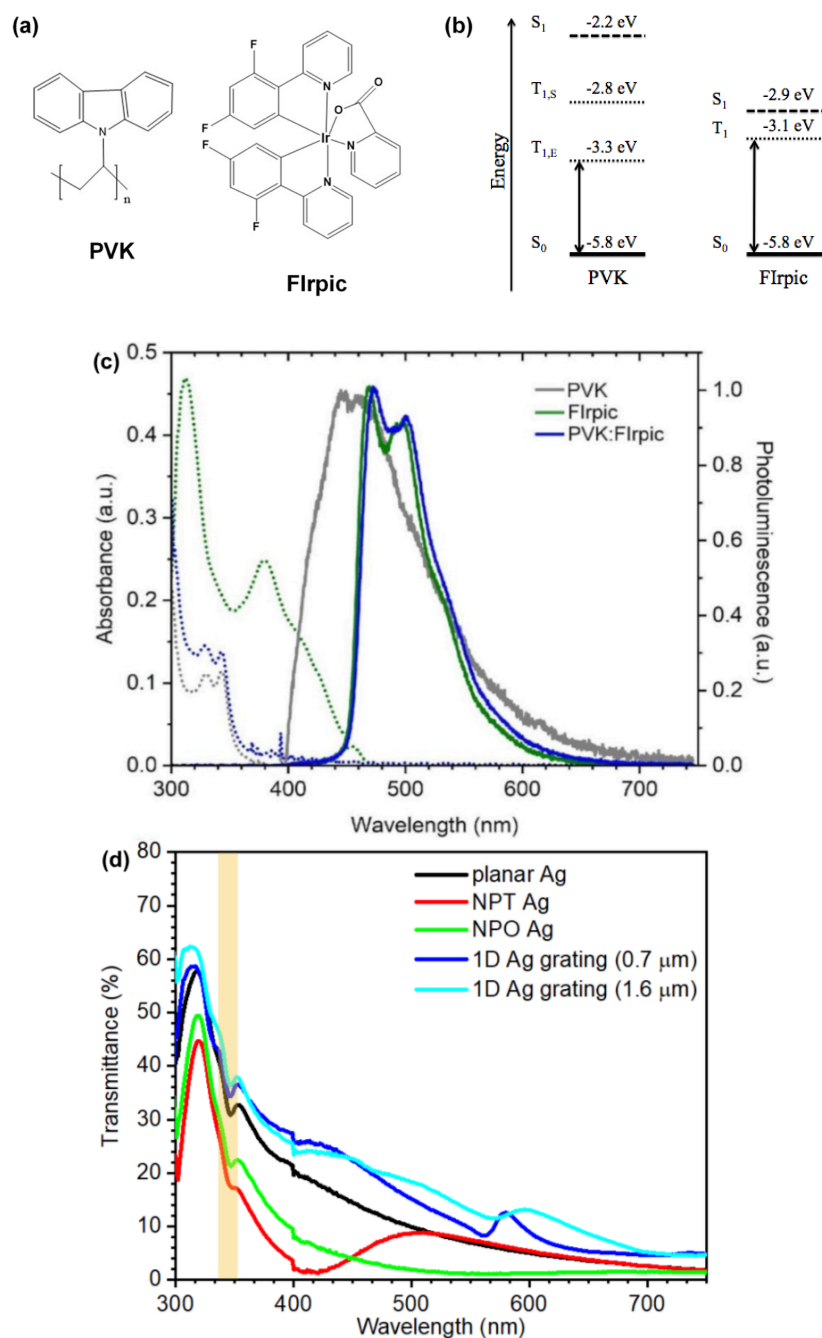


**Figure 2.2.** (a) Molecular structures of PVK and Flrpic. (b) Energy level diagram showing  $S_1$ ,  $T_{1,S}$ ,  $T_{1,E}$ , and  $S_0$  energy levels of PVK and Flrpic derived from Ref. [29, 30]. (c) Absorbance spectra (dashed curves) and intensity-normalized photoluminescence spectra (solid curves) of the host PVK, the dopant Flrpic, and the 9:1 blend PVK:Flrpic. A drop cast film of Flrpic was used to obtain the absorption spectrum of Flrpic (see Methods). All other spectra were obtained from spin coated thin films. Data obtained by Catrice Carter

and Rahma Leil. (d) Transmission spectra of PVK:FIrpic-coated Ag surfaces and of PVK:FIrpic-coated planar Ag. The yellow bar indicates the excitation wavelength range used for PL stability measurements. The average of two measurements was used for each transmission spectrum. All spectra were baselined at 900 nm except the NPT sample which is baselined at  $\sim 420$  nm. A small irregularity at 400 nm (the lamp crossover wavelength) occurred in all the spectra, due to a difference in the relative lamp intensities during the measurements.

wavelength range. The coated NPT Ag transmission spectrum showed a significant dip at  $\sim 410$  nm and a broad, pronounced transmission peak centered at 510 nm attributed to scattering from localized surface plasmon resonances (LSPR) of the nanoparticles. This peak was red shifted from the uncoated NPT surface due to the increase in the refractive index of the local environment of the PVK:FIrpic-coated nanoparticles, which causes a lowering in frequency LSPR of the shoulders (see Fig. 2.6). The coated NPO Ag did not exhibit notable peaks or shoulders in the visible wavelength range. The coated 1-D Ag gratings exhibited shoulders at  $\sim 450$  nm and peaks distributed across the visible and near-infrared wavelength range attributed primarily to grating modes. Given the significant change in the transmission spectra of the coated 1-D Ag gratings and NPT surfaces compared to coated planar Ag within the emission wavelength range of FIrpic (i.e., in the 450 nm to 550 nm wavelength range), these surfaces are expected to have the most noticeable effect on emission behavior of the PVK:FIrpic thin films.

Photoluminescence (PL) stability tests were carried out for PVK:FIrpic thin films on the various Ag surface and on planar Ag in order to investigate if the surfaces altered the photostability of the PVK:FIrpic emission. The PL stability tests were accelerated by using two excitation power densities,  $13.6 \text{ mW/cm}^2$  and  $136 \text{ mW/cm}^2$ . All PVK:FIrpic coated and uncoated Ag samples were passivated with an optical epoxy to eliminate

photooxidation during optical and photoluminescence measurements; see Methods. Without this passivation the stability of PVK:FIrpic thin films on all surfaces was dramatically lower. For example, at a UV excitation power density of  $136 \text{ mW/cm}^2$ , the time to reach 50% of initial intensity was a factor of 23 shorter for an unpassivated PVK:FIrpic thin film on glass compared to the passivated sample (Fig. 2.3).

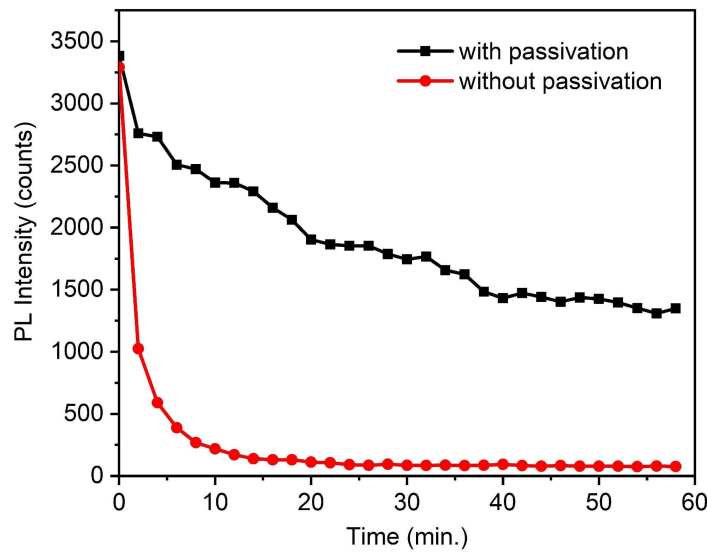


**Figure 2.3.** PL intensity versus UV exposure time for PVK:FIrpic thin films on glass substrates with and without passivation by epoxy and glass. Data acquired by Rahma Leil.

Representative PL stability results measured for an excitation power density of  $136 \text{ mW/cm}^2$  are shown in Figure 2.4a,b for PVK:FIrpic on a variety of Ag surfaces. It is apparent that the emission from PVK:FIrpic on the 1-D Ag gratings and on the NPT Ag was more stable relative to that on the planar Ag film. We define a stability enhancement factor to quantify the degree of improvement in PL stability of PVK:FIrpic films on Ag surfaces compared to the PL stability of PVK:FIrpic film on planar Ag as  $E_{90} = L_{90}(\text{surface})/L_{90}(\text{planar Ag})$  where  $L_{90}$  is the time it takes for the PL intensity to decay to 90% of its initial value. Other similar metrics,  $E_{70}$  and  $E_{50}$ , are also quantified using the



time it takes for PL intensity of the corresponding samples to decay to 70% and 50% of their initial intensities, respectively. Data taken from the fitted lines in Figure 2.4a showed similar trends in  $E_{90}$ ,  $E_{70}$  and  $E_{50}$  for each surface; therefore, the stability enhancement did not change significantly with time. Since the stability enhancement trends remain similar regardless of the % decay,  $E_{90}$  is chosen to be the metric of PL stability enhancement in the remainder of this study.

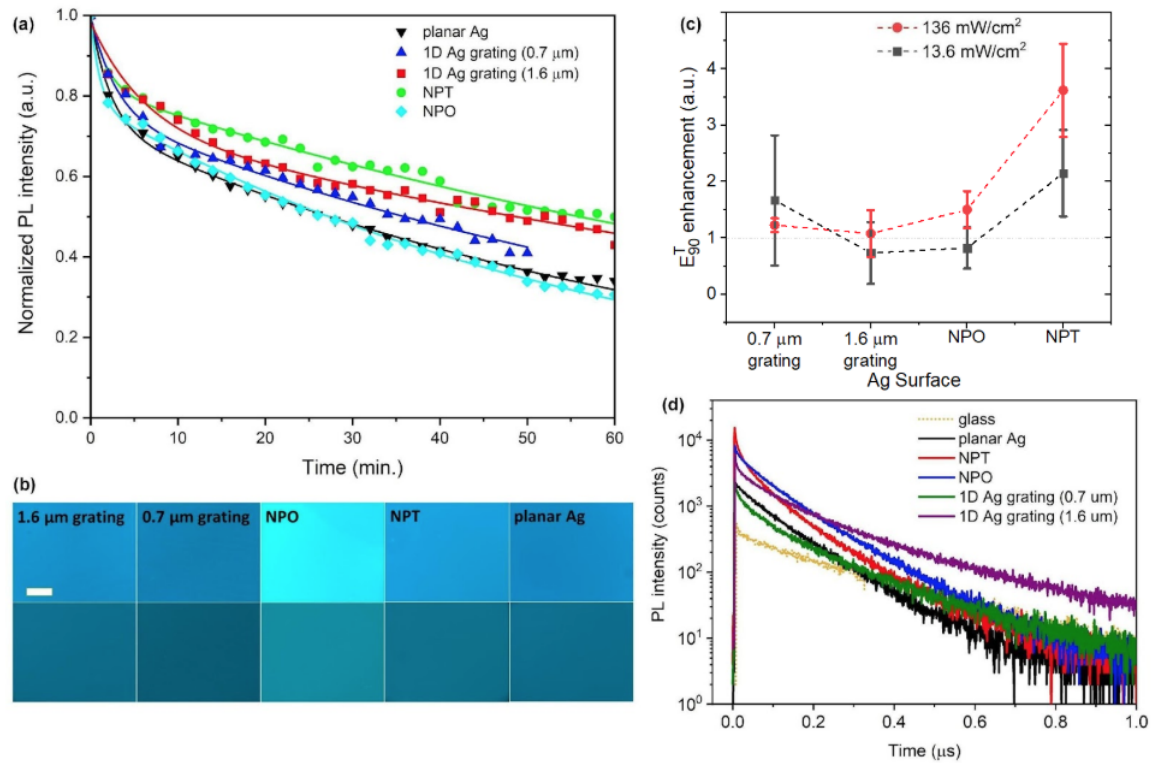


**Figure 2.4.** (a) Representative accelerated PL stability test of PVK:FIrpic thin films on various Ag surfaces. For the PL stability measurements, all samples were continuously exposed to focused UV light (wavelength  $365 \text{ nm} \pm 12 \text{ nm}$ ), with a power density of  $136 \text{ mW}/\text{cm}^2$  for 1 hour. The measured data is represented by symbols and exponential fits to the data are represented by the solid lines. No correction was carried out for differences in excitation power caused by variations in sample transmittance at the excitation wavelength. (b) PL images of PVK:FIrpic coated Ag surfaces, at 20x magnification, acquired

before (top row) and after (bottom row) stability measurements using the same conditions as (a). All images have the same image acquisition time and settings, and all images are on the same scale; the scale bar is 200  $\mu\text{m}$ . (c) Average stability enhancements ( $E_{90}^T$ ) averages (points) and standard deviations (error bars) for PVK:FIrpic coated Ag surfaces at two excitation powers 13.6  $\text{mW}/\text{cm}^2$  and 136  $\text{mW}/\text{cm}^2$ . For a particular excitation power the stability enhancement was normalized to the transmittance of the sample at the excitation wavelength (to correct for slight variations in excitation power due to differences in the transmittance of the samples); see Equation 1. The average  $E_{90}^T$  values were obtained from numerous stability measurements of each sample type as follows: four measurements of the 1.6  $\mu\text{m}$  1-D Ag grating, five measurement of the 0.7  $\mu\text{m}$  1-D Ag grating, five measurements of the NPO Ag, and three measurements of the NPT Ag at 13.6  $\text{mW}/\text{cm}^2$ . Two stability measurements of each Ag surface type were used at 136  $\text{mW}/\text{cm}^2$ . (d) Transient PL lifetime decay curves of PVK:FIrpic thin films on various surfaces. A 372 nm picosecond pulsed laser was employed for excitation and the measurements were carried out in reflection mode (Fig. 2.5). PL lifetime measurements were performed by Zeqing Shen.

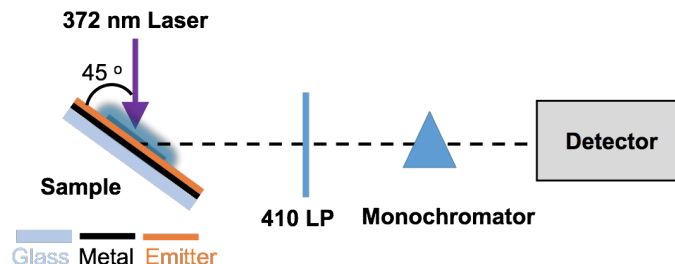


**Figure 2.5.** Schematic of experimental configuration used for transient PL lifetime measurements.

However, these stability measurements were not normalized for excitation power. Since there are variations in the transmittance of the coated surfaces at the excitation wavelength of 365 nm (Fig. 2.2b, Fig. 2.6-2.8), during the PL stability measurements, the PVK:FIrpic films are exposed to different excitation powers. This will impact the rate at which the PVK:FIrpic emission decays with time (i.e., its PL stability). For example, the 1-D Ag gratings have higher transmittances at the excitation wavelength compared to

planar Ag. This means that excitation light that is not absorbed by the PVK:FIrpic coating on its first pass through the coating, will not be reflected back into PVK:FIrpic by the gratings to the same degree as the planar Ag. Instead, more of the excitation light will be transmitted through the 1-D Ag gratings. As a result, the excitation power in the PVK:FIrpic film is expected to be lower for the 1-D Ag gratings compared to that for planar Ag. Hence, the PL stability enhancement of the 1-D Ag gratings is inflated. Conversely, NPO and NPT Ag surfaces exhibit lower transmittance compared to planar Ag at the excitation wavelength. Therefore, the excitation power in the PVK:FIrpic is expected to be greater on NPO and NPT Ag compared to that on planar Ag, due to more excitation light undergoing a second pass through the PVK:FIrpic thin film due to a higher reflectance.

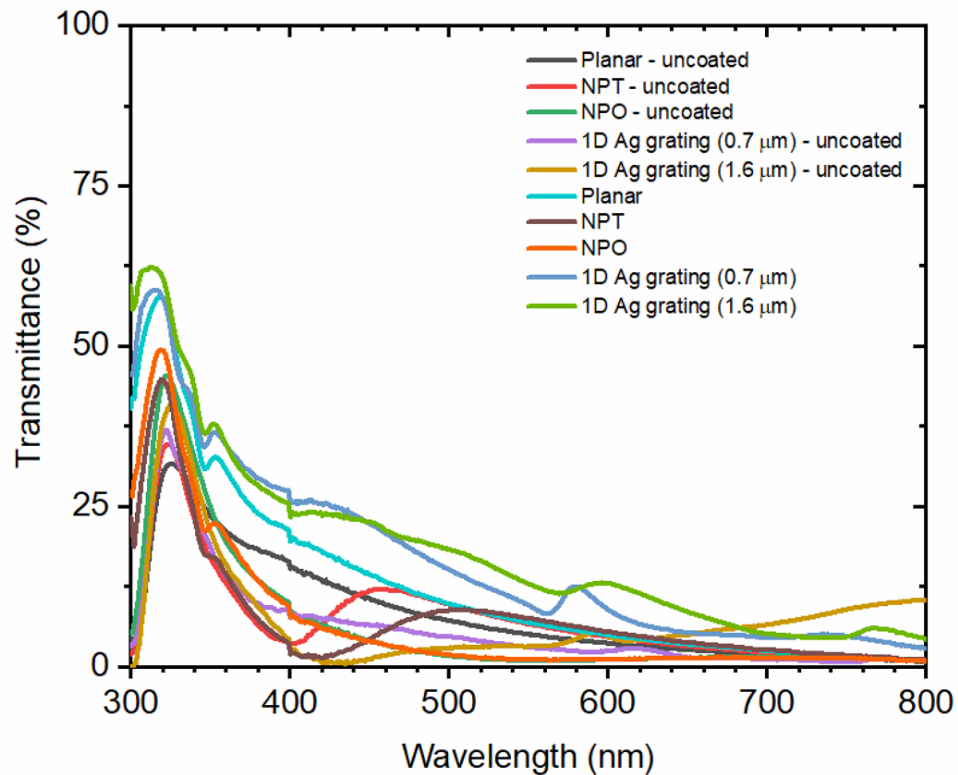


**Figure 2.6.** Transmittance spectra for different Ag (meta)surfaces with/without a PVK:FIrpic coating. All samples except the uncoated 1.6  $\mu\text{m}$  1-D Ag grating were baselined at 900 nm. The uncoated 1.6  $\mu\text{m}$  1-D Ag grating was baselined at  $\sim 425$  nm.

PVK:FIrpic absorbs in the ultraviolet spectral range; however, the transmittance of many of the metasurfaces increases when the silver metasurfaces are coated with PVK:FIrpic (Fig. 2.6). This indicates that the PVK:FIrpic film is acting, in-part, as an anti-reflective coating. The 1D Ag gratings and planar Ag transmit more with the coating, and the transmittance of NPT and NPO metasurfaces is only slightly affected by the coating. The red shift of the localized surface plasmon resonances of the NPT metasurface is apparent when coated with the PVK:FIrpic, as expected when the refractive index of the environment of the NPTs is increased.

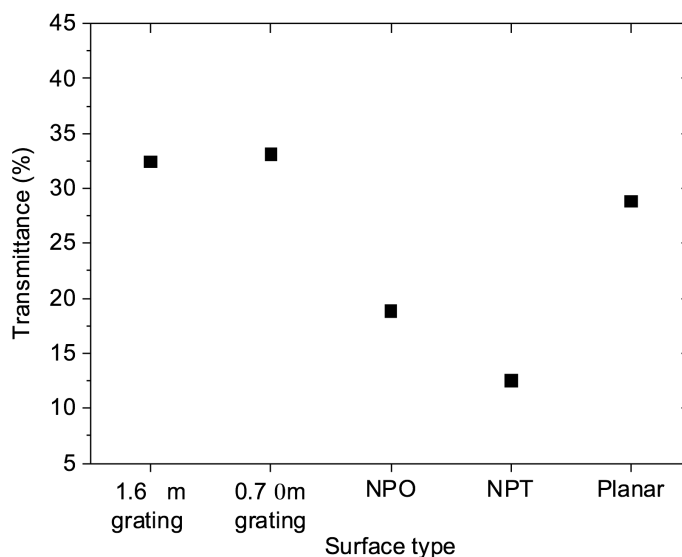


**Figure 2.7.** Transmittance for PVK:FIrpic coated Ag (meta)surfaces at a wavelength of 365 nm.

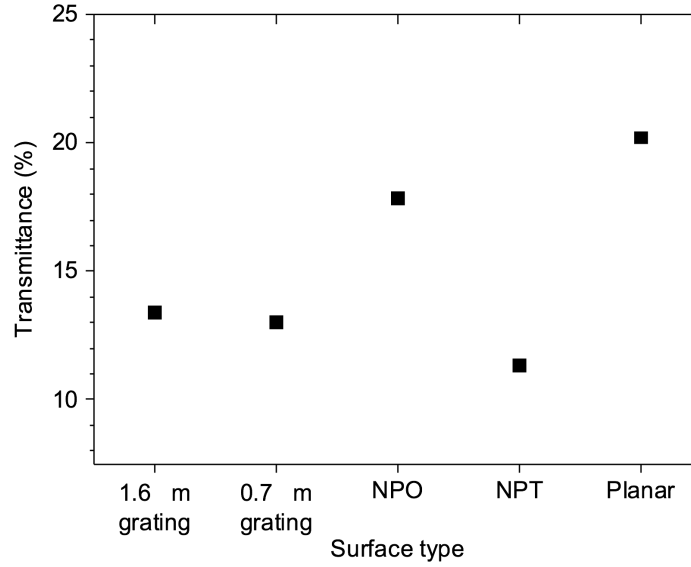


**Figure 2.8.** Transmittance for uncoated Ag (meta)surfaces at a wavelength of 365 nm.

Thus, to correct the stability enhancement values for excitation power differences, we calculated an excitation-power-corrected stability enhancement factor,  $E_{90}^T$ , defined as:

$$E_{90}^T = E_{90} \times \frac{T^{pAg}}{T^{meta}} \quad (1)$$

where  $E_{90}$  is the stability enhancement factor as defined earlier,  $T^{pAg}$  is the transmittance of silver, and  $T^{meta}$  is the transmittance of the surface. The transmittance factor,  $T$ , is represented as  $\frac{T^{pAg}}{T^{meta}}$ . Figure 2.4c shows stability enhancement values for each surface that were normalized for excitation power, as described above. Additionally, the enhancement values are averages of multiple stability measurements from each sample type. Clearly, once normalized for excitation power, the 1-D gratings no longer exhibited the greatest stability enhancement because of their high transmittance (Fig. 2.2b, 2.3a and Equation

1). Instead, the NPT surfaces cause the greatest stability enhancement. In general, the enhancement in stability by all surfaces is greater at the higher excitation power (Fig. 2.4c). We expect greater TTA to occur at higher excitation powers due to the increase in the triplet population. The surfaces are likely to have a greater impact on stability when there is significant TTA due to their ability to accelerate triplet radiative decay rate and thereby reducing the population of triplets that can take part in TTA. The observed power-dependent behavior is consistent with our original hypothesis that when there is an increase in the phosphorescence decay rate, an increase in the phosphorescence stability can occur, especially when there is a large population of excited triplet states. The trend in  $E_{90}^T$  between different surface types remains similar at both excitation powers. At high power, all the surfaces cause a phosphorescence stability enhancement when compared to planar silver Ag. NPT Ag consistently resulted in the most stable PVK:FIrpic emission, with average stability enhancement factor of 3.6.

Transient PL lifetime testing for PVK:FIrpic on each Ag surface type was used to determine if enhanced PL stability correlates with enhanced PL lifetime (Fig. 2.4d). The long average PL lifetime decay constant ( $\tau_{PL} = 0.96 \mu\text{s}$ ) of PVK:FIrpic when on glass can be attributed primarily to the natural phosphorescence lifetime decay of the dopant FIrpic. Overall, PVK:FIrpic thin films on metallic surfaces shortens the average PL lifetime,  $\tau_{PL}$  (by a factor of up to 2.8) compared to that on glass. Further, there is an apparent increase in the maximum PL intensity compared to PVK:FIrpic on planar Ag for PVK:FIrpic on all Ag surfaces, with NPT causing the greatest increase in PL intensity. The initial PL intensity enhancement,  $E_{PL}$  (i.e., the PL intensity at a time of 0 s for PVK:FIrpic on the surface divided by that on planar Ag), is a measure of quantum

efficiency enhancement assuming all radiated PL is collected by the measurement optics. The  $E_{PL}$  is 6.6 on NPT, 3.5 on NPO, 2.7 on 1.6  $\mu\text{m}$  1-D Ag grating and 1.1 on 0.7  $\mu\text{m}$  1-D Ag grating (values are relative to planar Ag).

Substrate	$\tau_{PL}$ ( $\mu\text{s}$ )	PL Intensity @ $t = 0$ s (counts)	$\tau_1$ ( $\mu\text{s}$ )	$\tau_2$ ( $\mu\text{s}$ )	$\tau_3$ ( $\mu\text{s}$ )	$\chi^2$
Glass	0.96	477	0.17 (24%)	1.01 (75%)	-	0.93
Planar Ag (2 <sup>nd</sup> order fit)	0.44	2333	0.30 (74%)	0.62 (26%)	-	0.98
Planar Ag (3 <sup>rd</sup> order fit)	0.45	2333	0.15 (24%)	0.42 (73%)	1.09 (3%)	0.87
1-D Ag Grating (1.6 $\mu\text{m}$ )	0.80	6186	0.07 (32%)	0.46 (54%)	1.32 (14%)	1.01
1-D Ag Grating (0.7 $\mu\text{m}$ )	0.64	2608	0.07 (40%)	0.41 (49%)	1.15 (11%)	1.02
NPT Ag	0.34	15319	0.04 (43%)	0.22 (42%)	0.55 (15%)	0.96
NPO Ag	0.42	8222	0.05 (21%)	0.32 (59%)	0.62 (20%)	1.04

**Table 2.1.** The average PL lifetime ( $\tau_{PL}$ ), intensity at time,  $t = 0$  s, shortest PL lifetime decay component ( $\tau_1$ ), longer PL lifetime decay component ( $\tau_2$ ), and the longest PL lifetime decay component ( $\tau_3$ ) for PVK:Flrpic thin films on glass, planar Ag, 1.6  $\mu\text{m}$  1-D Ag grating, 0.7  $\mu\text{m}$  1-D Ag grating, NPT Ag

metasurfaces and NPO Ag metasurfaces. The PL lifetime components were extracted from fits to the data using a second or third order exponential decay functions. The percentage contributions of each lifetime component to the average PL lifetime are shown in parentheses.

The PL lifetime decay curves were fit with multiexponential decay functions to analyze the various decay components of the lifetime curves. The results show that in all cases that there are fast and slow lifetime decay time constants, which contribute to the overall shape of the decay curves (i.e., PL lifetime decay curves were best fit with double or triple exponential decay functions); Table 2.1. The PL lifetime of PVK:FIrpic on planar Ag has two components with time constants of 0.3  $\mu\text{s}$  and  $\sim 0.6 \mu\text{s}$ . There is a new fast initial exponential decay on both 1-D Ag gratings ( $\tau_1 \simeq 0.07 \mu\text{s}$ ) and an even faster initial decay on NPT surfaces ( $\tau_1 \simeq 0.04 \mu\text{s}$ ), not observed on planar Ag, which contribute significantly (30% - 43%) to the average PL lifetime. This fast component is also observed on NPO but it has a less significant contribution to the average lifetime (21 %). The second fastest lifetime component on NPT ( $\tau_2 \simeq 0.2 \mu\text{s}$ ), NPO ( $\tau_2 \simeq 0.3 \mu\text{s}$ ), 0.7  $\mu\text{m}$  grating ( $\tau_2 \simeq 0.4 \mu\text{s}$ ) and 1.6  $\mu\text{m}$  grating ( $\tau_2 \simeq 0.5 \mu\text{s}$ ) are approximately the same time scale as the fastest PVK:FIrpic time constant ( $\tau_1 \simeq 0.3 \mu\text{s}$ ) on planar Ag, accounting for 40% - 60% of the average PL lifetime. However, while the longest component for the PVK:FIrpic on NPT and NPO ( $\tau_3 \simeq 0.6 \mu\text{s}$ ) is the same as the longest time constant ( $\tau_2 \simeq 0.6 \mu\text{s}$ ) of PVK:FIrpic on planar Ag, the third time constant for PVK:FIrpic on both gratings ( $\tau_3 \simeq 1 \mu\text{s}$ ) is much longer, possibly due to emitter-metal non-radiative interactions. As a result, the average PL lifetime of PVK:FIrpic on the Ag gratings ( $\tau_{PL} \simeq 0.6 \mu\text{s}$  and  $0.8 \mu\text{s}$ ) is lengthened compared to that on planar Ag. The average PL lifetime



of PVK:FIrpic on NPT ( $\tau_{PL} \approx 0.3 \mu\text{s}$ ) is the shortest of all samples measured and on NPO ( $\tau_{PL} \approx 0.4 \mu\text{s}$ ) PVK:FIrpic exhibits a similar lifetime to that on planar Ag.

Ag Surface Type	$E_{90}^T$		$\tau_{PL} (\mu\text{s})$	$E_{PL}$	$E_r$
	$13.6 \text{ mW/cm}^2$	$136 \text{ mW/cm}^2$			
planar Ag	1.00	1.00	0.44	1	1
1-D Ag grating (1.6 $\mu\text{m}$ )	$0.74 \pm 0.55$	$1.38 \pm 0.53$	0.80	2.65	1.46
1-D Ag grating (0.7 $\mu\text{m}$ )	$1.67 \pm 1.15$	$1.32 \pm 0.13$	0.64	1.12	0.77
NPO Ag	$0.82 \pm 0.36$	$1.66 \pm 0.36$	0.42	3.52	3.69
NPT Ag	$2.15 \pm 0.76$	$3.77 \pm 0.86$	0.34	6.57	8.50

**Table 2.2.** The excitation power corrected  $L_{90}$  stability enhancements (i.e.,  $E_{90}^T$ ), average PL lifetime ( $\tau_{PL}$ ), PL intensity enhancement ( $E_{PL}$ ) of PVK:FIrpic thin films on various Ag surfaces, and radiative decay rate enhancement ( $E_r$ ). Two different excitation power densities were employed for the stability measurements:  $13.6 \text{ mW/cm}^2$  and  $136 \text{ mW/cm}^2$ . Some  $E_{90}^T$  data was collected by Catrice Carter.

The PVK:FIrpic on 1-D Ag gratings has a long average PL lifetime, small or no radiative decay rate enhancement, and a slight PL stability enhancement when compared to that on planar Ag. This suggests that the stability enhancement mechanism does not originate from the Purcell effect. Evidence of the Purcell effect is shown by an increase in radiative decay rate which would occur when there is a decrease in PL lifetime of the PVK:FIrpic on the surface compared to that on planar Ag, and when there is an increase in the quantum yield (see Methods). NPO and NPT surfaces show a clear correlation between a decrease in PL lifetime, and an increase in PL stability and radiative decay

rate. The NPT surface exhibited the most intense and rapid PL lifetime and the greatest stability enhancement. Therefore, in the case of the PVK:FIrpic on NPT surface there is a strong correlation between enhanced stability and enhanced radiative decay rate relative to the PVK:FIrpic on planar Ag (Table 2). This correlation is consistent with a Purcell effect, which is causing an enhancement in the stability of PVK:FIrpic on NPO and NPT surfaces, as per our original hypothesis.

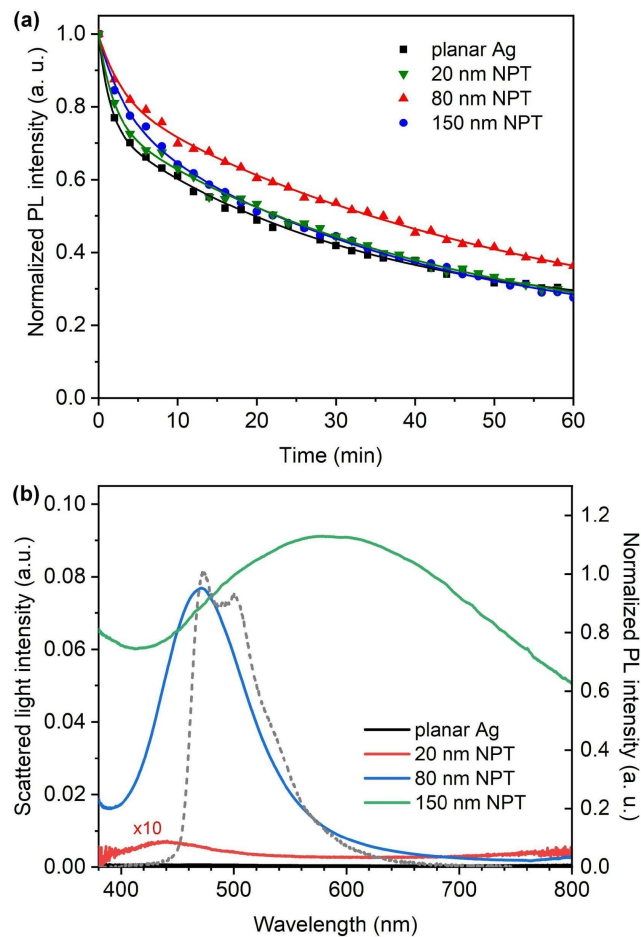


**Figure 2.9.** (a) Excitation-power-corrected accelerated PL stability curves of PVK:FIrpic thin films on various NPT Ag surfaces with different nominal NPT sizes and on planar Ag (50 nm). For the PL stability measurements, all samples were continuously exposed to focused UV light (wavelength  $365 \text{ nm} \pm 12 \text{ nm}$ ), with a power density of  $136 \text{ mW/cm}^2$  for 1 hour. The PL stability curves were raised to the power of  $T$  (the

transmission correction factor), to correct for small differences in excitation power due to variations in sample transmittance at the excitation wavelength; see Methods. Data is represented by symbols and exponential fits to the data are represented by the solid lines. Nanoparticle fabrication performed by Zhongkai Cheng. (b) Scattered light spectra of PVK:FIrpic coated NPT Ag surfaces and planar Ag (solid curves). Also shown is the photoluminescence spectrum of a PVK:FIrpic film for comparison (dashed curve). The scattering spectrum of the 20 nm NPT surface was multiplied by a factor of 10 to show the shape of the spectrum. Dark field spectra conducted by Rahma Leil.

To investigate the effects of NPT size on the phosphorescence stability of PVK:FIrpic thin films, PL stability measurements were carried out for PVK:FIrpic thin films coated on NPT Ag surfaces with NPT sizes. The NPT size was varied by changing the initial thickness of the Ag film that was thermally dewetted and subsequently evaporating Ag on top of the NPTs such that the total thickness of evaporated Ag was 50 nm; see Methods. The size of the NPTs were nominally 20 nm, 80 nm and 150 nm, based on average sizes determined from SEM images. Figure 2.9a shows the PL stability results for the various NPT surfaces that were corrected for excitation power variations. It is apparent that the NPT Ag surface with nominal particle size of 80 nm is more effective at improving the phosphorescence stability of PVK:FIrpic compared to the other NPT and planar Ag surfaces. This is attributed to the improved spectral overlap of the surface plasmon resonances of the 80 nm NPT Ag surfaces with the emission spectrum of the PVK:FIrpic (Fig. 2.9b and Fig. 2.10). Surface plasmon resonances both scatter and absorb light at their resonance wavelength; therefore, peaks in the scattered light spectrum are indicative of the wavelength of the surface plasmon resonances. It is apparent that the 80 nm NPT Ag surface has the best spectral overlap with the emission

of the PVK:FIrpic films compared to the other NPT surfaces. This further supports the role of surface plasmon resonances in improving phosphorescence stability.

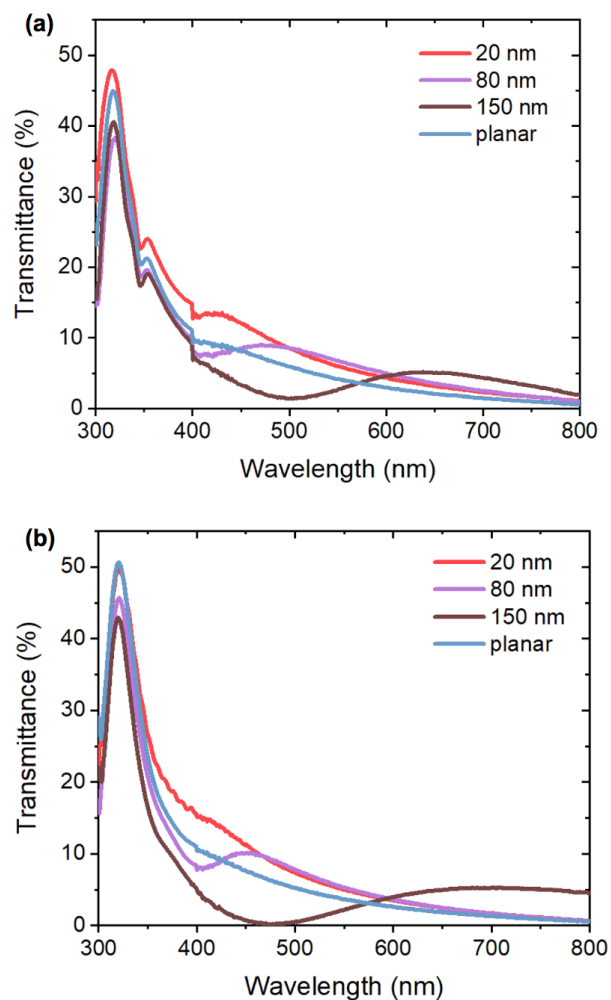


**Figure 2.10.** Transmittance spectra for (a) PVK:FIrpic coated NPT metasurfaces of varying NPT diameter (nominally, 20 nm, 80 nm and 150 nm), and (b) uncoated NPT metasurfaces of varying NPT diameter. Also shown is the transmittance of corresponding planar Ag samples. All spectra are baselined at 900 nm except the 150 nm sample, which is baselined at  $\sim 475$  nm. The total thickness of Ag deposited on all surfaces was 50 nm.

### 2.3.1. Extrapolation to an OLED Device:

While our results are fundamental in nature and show that the plasmonic properties of surfaces can be useful in improving the stability of blue organometallic phosphors; it may be of interest to consider how these results could affect a practical application such as OLED displays or lighting. However, the OLED industry uses luminance (in  $\text{cd/m}^2$ ) rather than power density (in  $\text{mW/cm}^2$ ) as a measure of emitted optical brightness. To convert from power density to luminance a standard radiometric to photometric conversion can be applied (see Methods). Based on this conversion, the excitation power densities used in this study,  $13.6 \text{ mW/cm}^2$  and  $136 \text{ mW/cm}^2$ , are equivalent to luminances of approximately  $10,000 \text{ cd/m}^2$  and  $100,000 \text{ cd/m}^2$ , assuming the emitter has a quantum yield of 100%. These luminance values are factors of 10 and 100 greater than standard for OLED stability testing ( $1000 \text{ cd/m}^2$  [31-33]).

To extrapolate the PVK:Firpic film's stability measured in this work to a  $1000 \text{ cd/m}^2$  OLED setting, we employed a conversion approach reported by Zhang et al., as follows:

$$L_{50}(1000 \text{ cd/m}^2) = L_{50}(X \text{ cd/m}^2) * \left[ \frac{(X \frac{\text{cd}}{\text{m}^2})}{1000 \frac{\text{cd}}{\text{m}^2}} \right]^n \quad (2)$$

where  $L_{50}$  is the time it takes to get to 50% of the initial luminance,  $X$  is the luminance value of interest, and  $n$  is a constant equal to 1.55 [33]. So, using the transmission-corrected  $L_{50}$  data derived from Figure 2.4a (i.e., the measured  $L_{50}$  of PVK:Firpic on a surface divided by the transmission factor), the  $L_{50}$  at  $1000 \text{ cd/m}^2$  would be  $1.7 \times 10^3$  hours,  $8 \times 10^2$  hours,  $8.2 \times 10^2$  hours, and  $5.7 \times 10^2$  hours for PVK:Firpic on NPT, NPO,  $1.6 \mu\text{m}$  1-D Ag grating,  $0.7 \mu\text{m}$  1-D Ag grating, and planar Ag surfaces, respectively.

Therefore, at  $1000 \text{ cd/m}^2$ , we project that the PVK:FIrpic on the NPT surface has a  $L_{50}$  that is at least a factor of two times greater than on the other surfaces, and all surfaces caused improved phosphorescence stability compared planar Ag. The projected  $L_{50}$  of PVK:FIrpic on planar Ag at  $1000 \text{ cd/m}^2$  in this study is very similar to that reported for blue-emitting, iridium (III) tris[3-(2,6-dimethylphenyl)-7-methylimidazo[1,2-f]phenanthridine], Ir(dmp)<sub>3</sub>, based phosphorescent OLEDs made by Zhang et al [33]. This indicates that our projected  $L_{50}$  at  $1000 \text{ cd/m}^2$  values are reasonable. Yet a number of assumptions were made to obtain those projected stability values, as follows.

There are several assumptions in our projection of the  $L_{50}$  stability in an OLED setting. First, we assumed the quantum yield of PVK:FIrpic is 100%. Second, to make the comparison between the photoexcited PVK:FIrpic and an electrically excited OLED, it is assumed that photoluminescence and electroluminescence equally populate the triplet state. Additionally, even if there is an equal population of initial excited triplet states, OLEDs experience TPA, so there may be less photon emission from OLEDs and, therefore, photoluminescence may have a higher triplet population. Finally, we assume that the electrical properties of the OLED will be unaffected by addition of nanostructures to a planar electrode. While these are significant assumptions, our estimate of the stability enhancement that would occur at  $1000 \text{ cd/m}^2$ , gives some insight into how the surface would perform in an OLED device. This fundamental study shows that plasmonic near fields can indeed impact the stability of blue organometallic phosphors. Significant work will be required to implement surfaces into OLED devices in a cost-effective way that does not otherwise compromise their high efficiency.

## 2.4. Conclusions

This fundamental study shows that plasmonic near fields can impact the photostability of blue organometallic phosphors. We investigated the use of silver plasmonic surfaces to increase the radiative decay rate of triplet emission from blue organometallic phosphorescent films, and, hence, to minimize triplet quenching processes that cause unstable emission. We demonstrate an improvement in the photostability of phosphorescence emission from blue organometallic OLED materials on a variety of different nanostructured silver surfaces compared to those on planar silver. Nanoparticle Ag surfaces exhibited the most significant increase in phosphorescence stability with an average enhancement factor of 3.6, along with a reduction in the average phosphorescence lifetime by a factor of 1.25, and an increase in intensity by a factor of 6.6 relative to the phosphor on planar Ag. However, at higher excitation powers, all of the Ag surfaces resulted in improved phosphorescence stability to different degrees. This study demonstrates that plasmonic surfaces are promising as electrodes for use in future phosphorescent OLED devices that require blue phosphorescence emission with improved stability.

## 2.5. Methods

### 2.5.1. Preparation Organic Thin Films and Surfaces

To prepare thin films of poly(N-vinylcarbazole) (PVK) containing the blue phosphorescent dopant, bis[2-(4,6-difluorophenyl)pyridinato-C2,N](picolinato)iridium(III) (FIrpic), first, a PVK:FIrpic blend solution was prepared in

a 9:1 ratio (i.e., 10 wt% dopant concentration) to create a 20 g/L solution [10]. Stock solutions (15 mL or 5 mL quantities), were prepared of PVK and FIrpic in chlorobenzene in a flask/vial, to concentrations of 36 mg/mL and 4 mg/mL, respectively. Powders and solvents were weighed directly into a flask/vial on a scale for increased accuracy, and weights were adjusted as needed to achieve the desired ratio. To dissolve the PVK and FIrpic, the solutions were individually placed in a water bath on a hotplate and heated to 40 °C with 1000 revolutions per minute (rpm) spin speed for 10 minutes. A 5 mm x 2 mm polytetrafluoroethylene (PTFE)-coated magnetic stirring rod was used to assist with dissolution of the solid in chlorobenzene. Equal volumes of each stock solution were then added to a glass vial to prepare the PVK:FIrpic blend solution (10 mL or 2 mL quantities) with a total concentration of 20 mg/mL. The 9:1 host:dopant ratio is consistent with what has been previously shown in the literature for PVK:FIrpic thin films.

The PVK:FIrpic blend solution was then used to prepare PVK:FIrpic thin-films on various surfaces by spin coating the blend solution using the following parameters: 100  $\mu$ L drop volume, 2000 rpm spin speed, 25 s spin time. The samples were then dried for 19 to 21 hours in a vacuum desiccator. After drying, PVK:FIrpic thin films were passivated by bonding a glass coverslip to the films using optical adhesive. Using the wooden end of a cotton swab, a small dot (approximately pea sized) of optical adhesive was put onto the film. A clean piece of thin glass was then placed on top of the adhesive and pressed upon with tweezers. The optical adhesive was then cured under a UV light for 5 minutes. Passivation is used to reduce photooxidation. Four different types of Ag (meta)surface were fabricated: planar Ag; nanoimprinted 1-D Ag gratings with 1.6  $\mu$ m period and 0.7  $\mu$ m period; nanoporous (NPO) Ag, and nanoparticle (NPT) Ag.



The Ag metasurfaces were prepared using the following nanofabrication methods. Nanoimprint lithography was employed for fabrication of 1-D Ag gratings with 1.6  $\mu\text{m}$  and 0.7  $\mu\text{m}$  period. A polydimethylsiloxane (PDMS) silicone elastomer with a base to curing ratio of 10:1 was created through constant mixing to ensure effective crosslinking. Then, a cleaned 1.6  $\mu\text{m}$  and 0.7  $\mu\text{m}$  grating disk from a CD or DVD was placed into a petri dish with the viscous PDMS and annealed in an oven at 130  $^{\circ}\text{C}$  for 30 minutes in an ambient environment. Once cooled the petri dish was removed from the oven, the PDMS mold was removed from the petri dish and cut into 2 cm x 2 cm squares. A poly (methyl methacrylate) (PMMA) film was created by spin coating PMMA solution (5 wt% in chloroform) onto clean coverslip glass with the following spin coating parameters: 6000 rpm, 60 seconds, and 20  $\mu\text{L}$ . The 2 cm x 2 cm PDMS mold was then placed on top of the PMMA film with imprint side face down to ensure grating transfer. The PDMS mold/PMMA film combination was then placed on a metal slab and an additional metal slab with weights ( $\sim 5$  kg) was placed on top. It was then placed back into the oven and annealed at 170  $^{\circ}\text{C}$  for 2.5 hours. Once cooled, the sample was removed and the PDMS mold was removed from the grating-imprinted PMMA film. Subsequently, Ag was thermally evaporated to a thickness of 50 nm on the grating-imprinted PMMA film to create a 1-D Ag grating metasurface.

Thermally-assisted dewetting of silver thin films was employed for the fabrication of NPO and NPT Ag metasurfaces [34] with an effective thickness of 50 nm of silver for both studies. The NPO Ag metasurfaces were fabricated using the following method: 50 nm of Ag was thermally evaporated onto a cleaned glass coverslip; then, the Ag coated coverslip was placed in an argon filled glovebox and annealed at 200  $^{\circ}\text{C}$  for 20 minutes

on a hotplate; finally, the sample was allowed to cool to room temperature. NPT Ag metasurfaces were prepared using a similar method to the NPO Ag metasurfaces but with differences in the metal deposition step and in the temperature and duration of the anneal. First, 10 nm of Ag was thermally evaporated onto a clean glass coverslip and the Ag-coated glass was placed into an argon-filled glovebox. The sample was then annealed at 540 °C for 5 minutes to form NPTs by thermally-assisted dewetting. Subsequently, the sample was allowed to cool to room temperature. Finally, the sample was removed from the glovebox and 40 nm of Ag was thermally evaporated onto the substrate. This yielded NPT Ag metasurfaces with an average NPT diameter of ~80 nm. For the NPT Ag metasurface size-dependent study (Fig. 2.9), NPTs with three different average sizes were prepared by varying the Ag film thicknesses deposited before and after the anneal. To obtain average NPT sizes of 20 nm, 80 nm and 150 nm, Ag films of thickness 5 nm, 10 nm and 15 nm, respectively, were initially deposited by thermal evaporation onto clean glass coverslips. The same anneal conditions as above were applied. Subsequently, Ag film of thicknesses of 45 nm, 40 nm and 35 nm were deposited on the 20 nm, 80 nm and 150 nm Ag NPT samples, respectively, to create NPT Ag metasurfaces with a total effective Ag thickness of 50 nm.

The volume of metal used to fabricate the metasurfaces was kept consistent across all samples to an effective thickness of 50 nm. This was done to maintain a similar metasurface transmittance at the excitation wavelengths used for PL measurements, thus reducing the impact metallic film thickness variation may have on PL spectral results. However, some transmittance variations occurred even when controlling the amount of Ag because of differences in the optical properties of the metasurfaces when different

surface structures were employed. Hence, all PL measurements were normalized for transmittance (see below and main text). For all sample types, the silver metasurface quality and uniformity was investigated with scanning electron microscopy (SEM) and reflection-mode, dark-field (DF) optical microscopy. Further, UV-visible transmission and DF spectra were used to investigate the optical response of each Ag metasurface. A glass/optical adhesive/glass reference was used in between each transmission spectrum acquired from a particular Ag surface.

The aforementioned PVK:FIrpic solution and spin coating parameters were used to apply PVK:FIrpic thin films to the various Ag surfaces. The samples were passivated by bonding the film to a thin glass coverslip using UV-curable optical adhesive (NOA 63, Norland Products Inc.) applied directly onto dried PVK:FIrpic film. Passivation was necessary in order to reduce photooxidation and photobleaching, which can lead to excessive degradation of the PVK:FIrpic emission. For the uncoated metasurfaces and planar Ag samples, the adhesive was applied directly onto the Ag surface, and then a thin glass coverslip was bonded to the Ag surface by curing the adhesive under UV light with the same process described previously.

### ***2.5.2. Characterization of Organic Thin Films:***

The PVK:FIrpic film thickness was determined from an analysis of the absorbance spectra of planar PVK:FIrpic films on glass substrates. To extract film thickness from absorbance spectra, an adapted version of Beer-Lambert's law for solids was employed, which consisted of the following equations:

$$A = \log[1/T]; x = \ln[T]/-\alpha \quad (3)$$

$$\alpha = 4 \pi k / \lambda \quad (4)$$

where  $\alpha$  is the absorption coefficient,  $A$  is absorbance,  $T$  is transmittance,  $x$  is PVK:FIrpic film thickness, and  $k$  is the imaginary part of the refractive index (i.e., extinction coefficient). Using those equations, the measured absorbance spectra and  $\alpha = 46,675 \text{ cm}^{-1}$  (based on the extinction coefficient of PVK reported in Ref. [30]), we found the PVK:FIrpic films on glass to have a thickness of  $62 \text{ nm} \pm 8.1$ . This thickness was confirmed by atomic force microscopy (AFM) line profile measurements.

For measurements of absorbance spectra (Fig. 2.2c), films of FIrpic were prepared by drop casting, instead of by spin coating, because spin coated films of FIrpic did not show detectable absorption peaks due to their thinness and the low solution concentration. Drop cast FIrpic films were prepared by dropping 100  $\mu\text{L}$  of a 2 mg/mL FIrpic solution in chlorobenzene onto a cleaned glass coverslip, and subsequent drying for 19 to 21 hours in a fume hood. PVK:FIrpic and PVK thin films were prepared by spin coating according to the methods described above. The concentration of the PVK solution for spin coating PVK thin films was 18 mg/mL. All of the samples were passivated with optical adhesive and glass coverslips. UV-visible (UV-vis) absorbance and transmission spectra were obtained using an SI Photonics CCD Array UV-visible absorption spectrometer with high precision. A lamp crossover wavelength of 370 nm was used for the measurements of PVK:FIrpic and PVK thin films, and a crossover wavelength of 450 nm was used for the measurements of FIrpic thin films. A glass/optical adhesive/glass reference was used for absorbance and transmission measurements and a reference measurement was always carried out before each absorption/transmission spectroscopy measurement of the samples.

### ***2.5.3. Photoluminescence Characterization Methods***

PL stability measurements were carried out using time-dependent PL spectroscopy of PVK:FIrpic films on various (meta)surfaces by acquiring a PL intensity spectrum every 2 minutes for a duration of up to 2 hours from a location of a particular sample using an epi-fluorescence microscope (Axio Vert.A1, Carl Zeiss Microscopy, LLC; excitation wavelength of  $365 \text{ nm} \pm 6 \text{ nm}$ , using a 120 W Hg vapor short arc lamp (X-Cite 120Q, Excelitas Technologies)). A previously unexposed location of the sample was used at the beginning of each stability measurement and multiple stability measurements were carried out on each different sample type. Two different excitation powers densities were employed for PL stability measurements using the epi-fluorescence microscope:  $13.6 \text{ mW/cm}^2$  and  $136 \text{ mW/cm}^2$ . Power readings were acquired before and after a particular stability measurement and the two readings were averaged to give a measure of the excitation power. The lamp excitation power varied by less than 6% over the duration of the stability measurements. The area of the excitation spot to which the sample was exposed was determined by taking a calibrated microscope image of the excitation spot and measuring the spot's area on ImageJ. Then, the excitation power density was calculated by dividing the averaged excitation power by the area of the excitation spot.

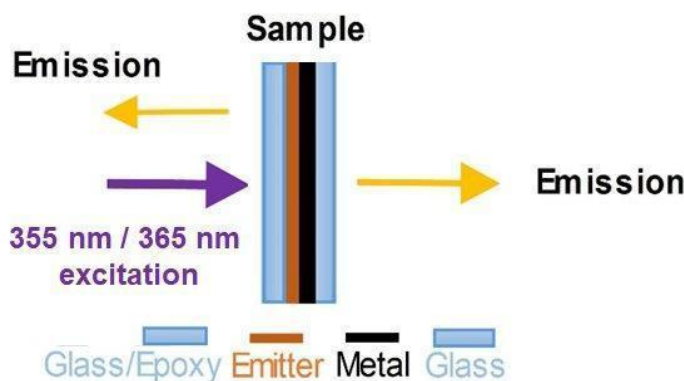


**Figure 2.11.** Schematic of the sample configurations used for the PL stability measurements. Two stability configurations were used. One was in epifluorescence mode, where 365 nm Hg arc lamp excitation was incident on the glass/epoxy/emitter side of the sample and the emission was collected from the same side of the sample (as shown above). The other configuration was in transmission mode, where 355 nm laser excitation was employed on the glass/epoxy/emitter side of the sample (as before), and the emission was collected from the opposite side of the sample (i.e., the metal/glass side). The epoxy was a UV-curable optical adhesive (NOA 63, Norland Products Inc.).

Another method was employed for PL stability measurements in transmission mode using 355 nm laser excitation and a 400 nm long pass filter in the collection optical path (Fig. 2.11). The average laser excitation power reading was taken during each spectral acquisition step to account for laser intensity fluctuations with time. The typical laser excitation power density and repetition rate were approximately  $\sim 10 \text{ mW/cm}^2$  and 100 Hz to 1000 Hz (varied to obtain a particular luminance at the sample). For PL stability measurements acquired using 355 nm laser excitation, the PL intensity spectrum was divided by the laser power recorded for each respective PL intensity spectrum. In both the epifluorescence-mode and transmission-mode PL stability measurements described above the excitation light was always incident on the PVK:FIrpic thin film before the metal surface.

Although these metasurfaces caused PVK:FIrpic phosphorescence stability enhancements relative to planar Ag, the phosphorescence stability was reduced by a factor of 2 relative to PVK:FIrpic on glass. The reduced stability on metal substrates compared to glass stems from the stability measurement geometry whereby there was increased excitation power in the PVK:FIrpic on metal samples due a double pass of the excitation light back into the PVK:FIrpic thin film due to reflected excitation light that was not absorbed on the first pass through PVK:FIrpic (Fig. 2.11). It should be noted that within optoelectronic devices, PVK:FIrpic thin films will be in the presence of metallic electrode surfaces thus the stability comparison with PVK:FIrpic on planar Ag rather than on glass is more appropriate.

Dark-field scattering spectra were acquired in reflection mode using an inverted microscope (Axio Vert.A1, Carl Zeiss Microscopy, LLC) equipped with a dark-field filter cube and dark-field microscope objectives. A Xenon lamp was used for dark-field illumination and spectra were acquired using the imaging spectrometer with an exposure time of 0.01 s for 500 accumulations. Subsequently, dark-field spectra of the samples were processed as follows to remove background light and to correct for the shape of the lamp spectrum:

$$I = \frac{I_{sample} - I_{background}}{I_{lamp} - I_{background}} \quad (5)$$

where  $I$  is the corrected dark-field scattering intensity spectrum,  $I_{sample}$  is the raw scattering intensity spectrum of the sample without being corrected,  $I_{background}$  is the scattering intensity spectrum of the background (i.e., with no lamp light incident on sample) and  $I_{lamp}$  is the scattering intensity spectrum of the lamp incident on a broadband diffuse reflector.

In Figure 2.9a, the plots of normalized PL intensity versus time were corrected for differences in excitation power as follows:  $I^* = I \cdot T$  where  $I^*$  is the corrected time-dependent PL intensity,  $I$  is the uncorrected time-dependent PL intensity and  $T$  is the transmission correction factor. The PL intensity versus time curves (i.e., the PL stability curves) were fit with an exponential decay function as follows:  $I = I_1 e^{-t/t_1} + I_2 e^{-t/t_2}$ , where  $t$  is time,  $t_1$  and  $t_2$  are decay times and  $I_1$  and  $I_2$  are initial intensities at  $t = 0$  s.

For PVK:FIrpic films on planar Ag the PL quantum efficiency  $\eta$  can be obtained from:

$$\eta = \frac{\Gamma_r}{\Gamma_r + \Gamma_{nr}} = \frac{\Gamma_r}{\Gamma_{total}} \quad (6)$$

where  $\Gamma_r$  is the radiative decay rate,  $\Gamma_{nr}$  is the non-radiative decay rate and  $\Gamma_{total}$  is the total decay rate. On a metasurface, the PL quantum efficiency, radiative and non-radiative decay rates of the PVK:FIrpic film may be modified compared to those on planar Ag. We can write the modified equation as follows:

$$\eta' = \frac{\Gamma_r'}{\Gamma_r' + \Gamma_{nr}'} = \frac{\Gamma_r'}{\Gamma_{total}'} \quad (7)$$

where  $\eta'$ ,  $\Gamma_r'$ ,  $\Gamma_{nr}'$  and  $\Gamma_{total}'$  are the modified PL quantum efficiency, radiative decay rate, non-radiative decay rate and total decay rate, respectively. The measured PL lifetimes,  $\tau_{PL}$ , can be used to obtain  $\Gamma_{total}$  and  $\Gamma_{total}'$  because

$$\Gamma_{total} = \frac{1}{\tau_{PL}} \quad (8)$$

and

$$\Gamma_{total}' = \frac{1}{\tau_{PL}'} \quad (9)$$



The modification of the quantum efficiency,  $E_\eta$  due to the metasurface relative to that on planar Ag can then be written:

$$E_\eta = \frac{\eta'}{\eta} = \frac{\Gamma_r' \times \Gamma_{total}}{\Gamma_{total}' \times \Gamma_r} = \frac{\Gamma_r' \times \tau_{PL}'}{\tau_{PL} \times \Gamma_r} = E_r \frac{\tau_{PL}'}{\tau_{PL}} \quad (10)$$

Assuming  $E_\eta \approx E_{PL}$ , we can estimate the radiative decay rate enhancement,  $E_r$  (where  $E_r = \frac{\Gamma_r'}{\Gamma_r}$ ); by rearranging Equation 10; see Table 2.

To estimate the luminance,  $B$  (in  $\text{cd/m}^2$ ), from the sample for a particular excitation power density in the PL stability measurements, we employed the following equation [35]:

$$B(\lambda) = V(\lambda) * n_{PL} * P_w * 683 * \pi \quad (11)$$

where  $\lambda$  is the emission wavelength, taken to be 450 nm,  $n_{PL}$  is the PL quantum efficiency of PVK:FIrpic (assumed to be 100 % [13]) and  $P_w$  is the average excitation power density in  $\text{W/m}^2$ . The constant 683 lm/W converts Watts to lumens and the factor  $\pi$  converts lumens to candela.  $V(\lambda)$  represents the photopic spectral luminous efficiency obtained from a non-linear regression fit to an experimental photopic spectral luminous efficiency curve with wavelength in units of micrometers [35]:

$$V(\lambda) = 1.019e^{-285.4(\lambda-0.559)^2} \quad (12)$$

PL intensity spectra were acquired using a Andor Shamrock SR 303i imaging spectrometer with an acquisition time of 0.5 s for low power excitation, and an acquisition time of 0.04 s for high power excitation (to prevent oversaturation of the spectra). When using laser excitation, the total acquisition time was 1 s (0.02 s exposure time, 50 accumulations) (Fig. 2.11). Planar PVK:FIrpic film on glass and on planar silver

were used as control samples. The intensity of the 0-1 excitonic transition from the FIrpic emission was extracted from the PL spectra and plotted versus time. The PL spectra acquired over the course of a PL stability measurement were intensity normalized to the initial maximum PL intensity value at the beginning of a stability measurement.

## 2.6. References

1. Gather, M. C., Koehnen, A., Meerholz, K. White organic light-emitting diodes. *Adv. Mater.* **23**, 233-248 (2011).
2. Jiang, W., Duan, L., Qiao, J., Dong, G., Zhang, D., Wang, L., Qiu, Y. High-triplet-energy tri-carbazole derivatives as host materials for efficient solution-processed blue phosphorescent devices. *J. Mater. Chem.* **21**, 4918-4926 (2011).
3. Fyfe D. Organic displays come of age. *Nat. Photon.* **3**, 453-455 (2009).
4. Liu, H., et al. Solution-processable hosts constructed by Carbazole/PO substituted tetraphenylsilanes for efficient blue electrophosphorescent devices. *Adv. Funct. Mater.* **24**, 5881-5888 (2014).
5. Qian, Y., Cao, F., Guo, W. High thermal stability 3, 6-fluorene-carbazole-dendrimers as host materials for efficient solution-processed blue phosphorescent devices. *Tetrahedron*, **69**, 4169-4175 (2013).
6. Zhang, Y., et al. Spiro-fused N-phenylcarbazole-based host materials for blue phosphorescent organic light-emitting diodes. *Org. Electron.* **20**, 112-118 (2015).
7. Xiang, C., Fu, X., Wei, W., Liu, R., Zhang, Y., Balema, V., Nelson, B., So, F. Efficiency roll-off in blue emitting phosphorescent organic light emitting diodes with carbazole host materials. *Adv. Funct. Mater.* **26**, 1463-1469 (2016).
8. Eersel, H., Bobbert, P.A., Janssen, R.A.J., Coehoorn, R. Monte Carlo study of efficiency roll off of phosphorescent organic light-emitting diodes: Evidence for dominant role of triplet-polaron quenching. *Appl. Phys. Lett.* **105**, 143303 (2014).
9. Baldo, M. A., Adachi, C., Forrest, S. R. Transient analysis of organic electrophosphorescence. II. Transient analysis of triplet-triplet annihilation. *Phys. Rev. B* **62**, 10967 (2000).
10. Zang, F. X., Sum, T. C., Huan, A. C. H., Li, T. L., Li, W. L., Zhu, F. Reduced efficiency roll-off in phosphorescent organic light emitting diodes at ultrahigh current densities by suppression of triplet-polaron quenching. *Appl. Phys. Lett.* **93**, 023309 (2008).
11. Giebink, N. C., Forrest, S. R. Quantum efficiency roll-off at high brightness in fluorescent and phosphorescent organic light emitting diodes *Phys. Rev. B* **77**, 235215 (2008).
12. Song, D., Zhao, S., Luo, Y., Aziz, H. Causes of efficiency roll-off in phosphorescent organic light emitting devices: Triplet-triplet annihilation versus triplet-polaron quenching. *Appl. Phys. Lett.* **97**, 243304 (2010).
13. Wang, J., Zhang, H., Ji, W., Zhang, H., Zhu, F. Origin of efficiency roll-off for FIrpic based blue organic light-emitting diodes and implications on phosphorescent molecule design. *Jpn. J. Appl. Phys.* **54**, 1016001 (2015).
14. Tao, Y., Yang, C., Qin, J. Organic host materials for phosphorescent organic light-emitting diodes. *Chem. Soc. Rev.* **40**, 2943-2970 (2011).
15. Lee, M. T., Lin, J. S., Chu, M. T., Tseng, M. R. Suppression of efficiency roll off in blue phosphorescent organic light-emitting devices using double emission layers with additional carrier-transporting material. *Appl. Phys. Lett.* **94**, 083506 (2009).
16. Yoo, S. I., Yoon, J. A., Kim, N. H., Kim, J. W., Kang, J. S., Moon, C. B., Kim, W. Y. Improvement of efficiency roll-off in blue phosphorescent OLED using double dopants emissive layer. *J. Luminesce.* **160**, 346-350 (2015).

17. Ji, W., Zhang, L., Xie, W. Improving efficiency roll-off in phosphorescence OLEDs by modifying the exciton lifetime. *Optics Lett.* **37**, 2019-2021 (2012).
18. Kim, S. H., Jang, J., Yook, K. S., Lee, J. Y. Stable efficiency roll-off in phosphorescent organic light-emitting diodes. *Appl. Phys. Lett.* **92**, 023513 (2008).
19. Reineke, S., Walzer, K., Leo, K. Triplet-exciton quenching in organic phosphorescent light-emitting diodes with Ir-based emitters. *Phys. Rev. B* **75**, 125328 (2007).
20. Hale, G. D., Jackson, J. B., Shmakova, O. E., Lee, T. R., Halas, N. J. Enhancing the active lifetime of luminescent semiconducting polymers via doping with metal nanoshells. *Appl. Phys. Lett.* **78**, 1502-1504 (2001).
21. O'Carroll, D. M., Hofmann, C. E., Atwater, H. A. Conjugated polymer/metal nanowire heterostructure plasmonic antennas. *Adv. Mater.* **22**, 1223-1227 (2010).
22. Kena-Cohen, S., Wiener, A., Sivan, Y., Stavrinou, P. N., Bradley, D. D. C., Horsfield, A., Maier, S. A. Plasmonic sinks for the selective removal of long-lived states. *ACS Nano* **5**, 9958-9965 (2011).
23. Chaudhuri, D., Li, D., Sigmund, E., Wettach, H., Höger, S., Lupton, J. M. Plasmonic surface enhancement of dual fluorescence and phosphorescence emission from organic semiconductors: effect of exchange gap and spin-orbit coupling. *Chem. Commun.* **48**, 6675-6677 (2012).
24. Ji, W., Zhang, L., Xie, W. Improving efficiency roll-off in phosphorescent OLEDs by modifying the exciton lifetime. *Opt. Lett.* **37**, 2019-2021 (2012).
25. Cang, H., Liu, Y., Wang, Y., Yin, X., Zhang, X. Giant Suppression of photobleaching for single molecule detection via the Purcell Effect. *Nano Lett.* **13**, 5949-5953 (2013).
26. Zhao, Y., et al. Efficiency roll-off suppression in organic light-emitting diodes at high current densities using gold bowtie nanoantennas. *Appl. Phys. Express* **20**, 022101 (2016).
27. Ma, D., Duan, L., Qiu, Y. Toward highly efficient blue organic light-emitting diodes: Fabricating a good-quality emissive layer cast from suitable solvents. *Dalton Trans.* **45**, 6118-6123 (2016).
28. Su, S., Takahashi, Y., Chiba, T., Takeda, T., Kido, J. Structure-property relationship of pyridine-containing triphenyl benzene electron-transport materials for highly efficient blue phosphorescent OLEDs. *Adv. Funct. Mater.* **19**, 1260-1267 (2009).
29. Jankus, V., Monkman, A. P. Is Poly(vinylcarbazole) a Good Host for Blue Phosphorescent Dopants in PLEDs? Dimer Formation and Their Effects on the Triplet Energy Level of Poly(N-vinylcarbazole) and Poly(N-Ethyl-2-Vinylcarbazole). *Adv. Funct. Mater.* **21**, 3350-3356 (2011).
30. Chang, J., An, J., Im, C., Kim, Y. K. Different Energy Transfer Behaviors of Poly (9-Vinylcabazole) and Polyfluorene Derivative Thin Films upon Doping with Triplet Emitters. *Journal of the Korean Physical Society*, **47**, 1028-1034 (2005). Fornasari, L., Floris, F., Patrini, M., Comoretto, D., Marabellia, F. Demonstration of fluorescence enhancement via Bloch surface waves in all-polymer multilayer structures. *Phys. Chem. Chem. Phys.* **18**, 14086-14093 (2016).
31. Fyfe D. Organic displays come of age. *Nat. Photon.* **3**, 453-455 (2009).
32. Lee, M. T., Lin, J. S., Chu, M. T., Tseng, M. R. Suppression of efficiency roll off in blue phosphorescent organic light-emitting devices using double emission layers with additional carrier-transporting material. *Appl. Phys. Lett.* **94**, 083506 (2009).

33. Zhang, Y., Lee, J., Forrest, S. R. Tenfold increase in the lifetime of blue phosphorescent organic light-emitting diodes. *Nat. Comm.* **5**, 5008 (2014).
34. Shen, Z., O'Carroll, D. M. Nanoporous Silver Thin Films: Multifunctional Platforms for Influencing Chain Morphology and Optical Properties of Conjugated Polymers. *Adv. Funct. Mater.* **25**, 3302-3313 (2015).
35. Light Emitting Diode Technologies, Radiometric vs. Photometric Units, Thorlabs Catalog, p 506. <https://www.thorlabs.de/catalogPages/506.pdf> (accessed April 19<sup>th</sup> 2019).

### **Chapter 3: FUTURE WORK**

In the future, the photoluminescent stability of organic blue phosphorescent material on discrete silver nanoparticles will be studied. The work in chapter 2 was done on continuous Ag nanoparticles on glass coated with PVK:Firpic. To further expand on this study, and to determine the impact of silver on stabilizing blue phosphorescent material, silver discrete nanoparticles on glass, and gold discrete nanoparticles NPT on glass will be studied. The PL stability of the discrete nanoparticles will be used to determine if silver or gold has a greater impact, or any impact, on increasing the stability of blue phosphorescent organic material (PVK:Firpic). It is anticipated that the silver will have a greater impact on stability because it emits best in the blue wavelength range, and gold emits at higher wavelengths (500-600 nm in Darkfield) compared to silver (red-shifted).

#### **3.1. Preliminary Data**

Preliminary photoluminescent stability data was taken (Figure 3.1). While the NPTs seem to have a greater initial decay, after that all samples are similar in decay rate (potentially even slightly better than PVK:Firpic). Au and Ag are very similar in their stability and rate of decay.

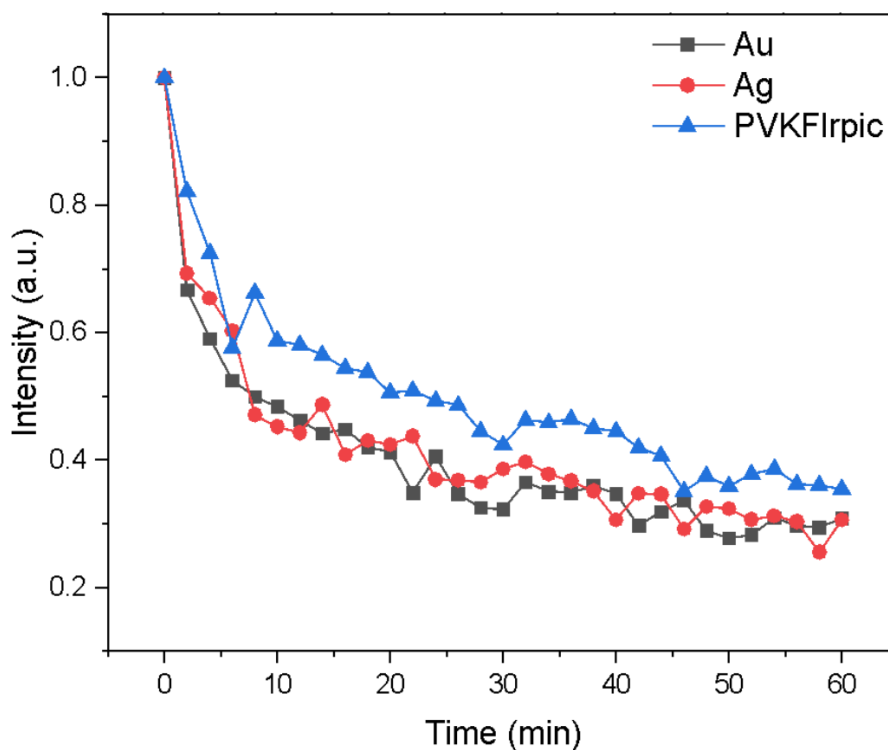


**Figure 3.1.** Photoluminescence stability measurements at 100,000  $\text{cd/m}^2$ .

The data must be adjusted for transmittance to determine the true stability trend, as described in chapter 2. In order to do so, the same steps will be used to test and analyze data as were used in chapter 2. Fresh samples will be prepared, UV-Vis data, PL Stability data, PL Lifetime, and QY data will all be collected. Some of these steps are described in the “Methods” section below.

## 3.2. Methods

### 3.2.1. Sample Preparation

The same solution preparation will be used as Chapter 2. The same glass cleaning procedure as in chapter 2 will be used. The glass substrates are completely immersed into

a Sparklene solution and sonicated for 10 minutes. After, the substrates are rinsed in three beakers of DI water (using tweezers cleaned in isopropanol). Next, the substrates are submerged into a 50/50 ethanol and hydrochloric acid solution (approximately 60 mL solution) for 15 minutes. Then, the substrates are rinsed in three beakers of DI freshwater (using tweezers cleaned in isopropanol). The substrates are then dried with a particle-free air gun and placed into a sample case. The substrates must be used within about an hour of cleaning, and cannot sit in a solution for a prolonged period of time because they will become dirty again.

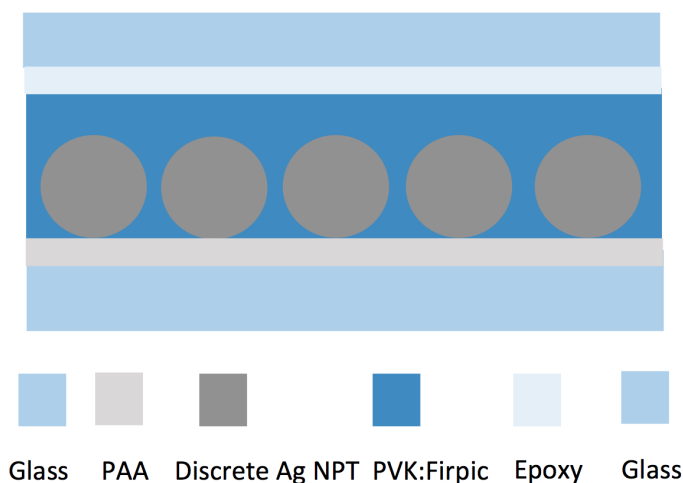


**Figure 3.2.** Discrete Ag NPT sample schematic.

Silver and gold nanoparticles with diameters of 60 nm were purchased (from nanoComposix) and spin coated onto PAA coated glass substrates. This step was carried out by Jill Tracey and is the same as that reported in her recent first author publication [1]. Subsequently, a thin film of PVK:Firpic was dynamically spin-coated in nitrogen onto a thin piece of microscope glass using the following spin coating conditions: 100  $\mu$ L drop volume, 2000 rpm, and 25 s spin time. This step was carried out by Rahma Leil. These conditions achieve a film thickness of 62  $\pm$  8.1 nm. No



bubbles should be in the pipette. New pipette tips are used after each sample injection. Samples were dried overnight in a desiccator with the sample case opened, but lightly surrounded by aluminum foil to prevent degradation caused by light. The same sample sealing procedure as Chapter 2 was used. A schematic of the sample structure can be found in Fig. 3.2.

The PVK:Firpic film thickness is determined using an adapted version of Beer-Lambert's law for solids:  $A = \log[1/T]$ ;  $x = \ln[T]/-\alpha$  and  $\alpha = 4 \pi k/\lambda$ , where  $\alpha$  is the absorption coefficient,  $A$  is absorbance,  $T$  is transmittance,  $x$  is PVK:Firpic film thickness, and  $k$  is the imaginary part of the refractive index (the extinction coefficient). The  $\alpha$  is a constant and is found to be  $\alpha = 46,675 \text{ cm}^{-1}$ . Thickness was confirmed by Zeqing Shen using AFM (atomic force microscopy) of a thin film on glass sample.

Reference samples are used to compare uncoated samples with the samples coated with PVK:Firpic. These are used to find the transmittance factor and for UV-Vis spectra. References include: uncoated Ag NPTs sealed with epoxy and glass, uncoated Au NPTs sealed with epoxy and glass, and glass epoxy glass. Unsealed and uncoated samples of both NPT types were also used.

### ***3.2.2. Optical Characterization and Spectroscopy***

The same procedure for acquiring absorption and transmission spectra as that used in Chapter 2 is required for this work. Photoluminescence stability measurements were carried out using time-dependent PL spectroscopy of PVK:Firpic films on Au and Ag discrete NPTs by acquiring a PL intensity spectrum every 2 minutes for a duration of

up to 2 hours from a location of a particular sample using an epifluorescence microscope (Axio Vert.A1, Carl Zeiss Microscopy, LLC; excitation wavelength of  $365 \text{ nm} \pm 6 \text{ nm}$ , using a 120 W Hg vapor short arc lamp (X-Cite 120Q, Excelitas Technologies)). The epifluorescence microscope was used instead of a laser because the microscope has a more continuous/steady excitation source. We studied the lamp excitation power's variations and found it varied by less than 6% throughout the study. The spot which the sample was exposed was to the excitation light was determined by taking an image of the excitation spot, calibrating the image using the scale bar on the picture, and measuring the spot's area on ImageJ (select the color, and adjust the scale bars on the side to cover the entire area of interest - the colored fluorescent shape).

The excitation power density used was  $136 \text{ mW/cm}^2$ , and is averaged over 1 s. This is equivalent to a luminescence of  $100,000 \text{ cd/m}^2$ , which is much higher than what is used in products on the market ( $\sim 1000 \text{ cd/m}^2$ ). The excitation power density was calculated by dividing the averaged excitation power by the area of the excitation spot. We expedite decay to determine the stability over time, and this stability can be extrapolated to determine the stability lifetime of the film in a real-life usage scenario.

The spectra were automatically collected through the Andors software in an FVB readout. The conditions were: 1 spectra every 2 min, total cycle duration 1 hour, exposure 1 s, 1 accumulation.

ZenCore microscope software was used to take an image of the sample before and after PL. After the picture is taken, the sample is moved slightly to a fresh region of the sample for the PL measurements to ensure accuracy. Images are taken in “manual” mode, so all of their image conditions are the same and have comparable intensities.

A previously unexposed location of the sample was used for each stability measurement. Power readings were acquired before and after a particular stability measurement and the two readings were averaged to give a measure of the excitation power. The same method will be used as described in Chapter 2 to correct for changes in transmittance between the samples at the excitation wavelength.

### 3.3 References

- 1) Tracey, J. I., O'Carroll, D. M., Short-Wavelength Lasing-Spasing and Random Spasing with Deeply Subwavelength Thin-Film Gain Media, *Adv. Funct. Mater.* **28**, 1802630 (2018).

## Chapter 4: OUTLOOK

The study of the impact of silver nanostructured metasurfaces on stabilizing blue phosphorescent material's stability should be further explored. The results that silver nanostructures increase photoluminescent stability raises more questions to be studied. The impact of the silver nanoparticles on other blue phosphorescent materials would be interesting to collect and compare to PVK:FIrpic. This will also show if the impact is the same for many different blue phosphorescent host-dopant blends.

Similarly, comparing the use of nanoparticles made from other noble metals and the phosphorescent materials that emit within the same wavelength as the metal could be studied. This would indicate if the increase in stability is a trend that remains across different materials and wavelength ranges.

A study to further explore the specific mechanism that is occurring to increase stability is also something that could be interesting to explore. For example, confirming if the Purcell Effect is in effect, and/or the impact/presence of radiative and non-radiative decay.

While the current commercial manufacturing of OLEDs has challenges, especially financially, testing the stabilization method in an OLED to see its viability is an important next step. If the nanostructured silver is able to still stabilize the blue phosphorescent material in an OLED, this would be a big success because then a completely phosphorescent OLED could be created. This would allow for a better image quality, and cheaper product use for customers.

In addition to being expensive to create, OLEDs are also expensive to purchase. Creating a large scale solution processing machine would be very helpful for OLED

production. Solution processing is significantly cheaper than thermal evaporation processing, so if companies were able to create OLEDs using solution processing methods (i.e. spin-coating), then OLEDs would be cheaper to purchase. Without a way to reduce the cost of OLEDs, their market share will be threatened by other flat-panel displays with improved image qualities, like quantum dot LEDs.